EPITAXIAL ALUMINUM OXIDE THIN FILMS ON NIOBIUM (110): A STUDY OF THEIR GROWTH AND THEIR USE IN SUPERCONDUCTING TUNNEL-JUNCTIONS

BY

PAUL BRENT WELANDER

B.A., Occidental College, 1999
B.S., California Institute of Technology, 1999

DISSERTATION

Submitted in partial fulfillment of the requirements
for the degree of Doctor of Philosophy in Physics
in the Graduate College of the
University of Illinois at Urbana-Champaign, 2007

Urbana, Illinois

Abstract

Epitaxial hetero-structures have been turned to in recent years in an attempt to eliminate charge fluctuations in Josephson junction-based quantum bits. Amorphous tunnel-barriers have large numbers of two-level fluctuators that can couple to the quantum states in the device. Single-crystal tunnel-barriers on the other hand show a reduced density of these two-level fluctuators. For my thesis research I studied the hetero-epitaxy of aluminum oxide on niobium, and the use of these aluminum oxide thin films as tunnel-barriers. Single-crystal Nb/Al_2O_3 and $Nb/Al_2O_3/Nb$ multilayers were grown by molecular beam epitaxy and characterized using a variety of materials analysis techniques. Atomically-flat niobium films grown on A-plane sapphire were used for the subsequent hetero-epitaxy of aluminum oxide. Depending on the thermal treatment used during growth, these niobium films had two distinct surface reconstructions. Using *in situ* RHEED I found that the growth of Al_2O_3 was highly dependent on the surface reconstruction of the underlying niobium film. Alumina films on *annealed* Nb had a hexagonal lattice that was under an isotropic tensile strain that relaxed with increasing film thickness. In contrast, alumina films on *unannealed* Nb showed an asymmetric strain and a pseudo-hexagonal lattice closely resembling that of the underlying niobium. Epitaxial niobium over-layers also tiled these two alumina surfaces differently, with in-plane orientations suggestive of irregular cation sublattices in the oxide film. It was also found using TEM imaging that an atomically sharp interface existed between the aluminum oxide film and the base niobium layer. However, mixing was seen to occur with the deposition

of the over-layer, causing a deterioration of the alumina barrier. This mixing had a profound effect on tunnel-junctions fabricated from these tri-layers. Devices showed very poor qualities overall, with current-voltage characteristics indicative of a large density of electrical pinholes. With these findings in mind, some potential solutions are proposed.

To Paula

Acknowledgments

First and foremost I would like to thank my research advisor, Prof. James Eckstein, for his support and guidance over the years, and for sharing with me his passion for physics. To former lab-mates Seongshik Oh and Maitri Warusawithana I want to express my gratitude for both their mentoring and their continued friendship. I hope I can serve those that follow me in the same manner that Seongshik and Maitri have served me. And to Soren Flexner and Dario Farias, also former group members, I will remember fondly our days as Gentlemen and Isotopes.

I also want to thank the growing number of current group members that I leave behind. First and foremost, I am deeply appreciative of the contributions of Tim McArdle, who fabricated and tested many of the tunnel-junction devices reported on in this thesis. I am grateful to both Kevin Inderhees and Stephanie Law, who provided invaluable support for a separate project not discussed here. To Mike Vissers I express my gratitude for his willingness to help me with just about anything, particularly system maintenance. I thank Xiaofang Zhai for her friendship and her humor. And to the newcomers, Chandra Mohapatra, Mao Zheng, and Allison Dove, I offer best wishes for a successful graduate tenure.

I also benefited greatly from the expertise of several CMM staff. I leaned heavily on Doug Jeffers and his technical knowledge of the EpiCenter MBE systems. Scott MacLaren, Mauro Sardela, and Rick Haasch also provided substantial assistance with their expertise in AFM, XRD and XPS, respectively. I also want to acknowledge Tony Banks and Kevin Colravy for their work in maintaining the instruments

in the MicroFab facility.

Others to thank include Prof. Dale van Harlingen, Trevis Crane, and Sergey Frolov for letting me use their sputtering system and for their assistance with tunnel-junction fabrication. I thank Prof. Jian-Min Zuo, Bin Jiang, and Amish Shah for carrying out TEM analysis of my epitaxial hetero-structures. I am also grateful to Prof. Angus Rockett for teaching me about XPS, both the technical and scientific aspects.

Finally, I want to thank my wife, Paula, for all of her support during graduate school, even while she pursued a doctoral degree herself. I thank my children, Katherine and Daniel, for enriching my life beyond measure. I am also deeply grateful to my parents, Gary and Barbara, for providing such a loving and nurturing home. It is the foundation that they laid which I stand upon today.

This research was funded by the National Science Foundation through Grant No. EIA 01-21568. Aspects of the research were carried out in the Center for Microanalysis of Materials, University of Illinois at Urbana-Champaign, which is partially supported by the U.S. Department of Energy under Grant No. DEFG02-91ER45439.

Table of Contents

List of Tables

List of Figures

List of Abbreviations

AES	Auger Electron Spectroscopy
AFM	Atomic Force Microscopy
bcc	Body-Centered Cubic
CMM	Center for Microanalysis of Materials
DAQ	Data Acquisition
ESCA	Electron Spectroscopy for Chemical Analysis
fcc	Face-Centered Cubic
IPA	Isopropyl Alcohol or Isopropanol
hcp	Hexagonal Close-Packed
HREELS	High-Resolution Electron Energy-Loss Spectroscopy
KS	Kurdjumov-Sachs
LEED	Low-Energy Electron Diffraction
MBE	Molecular Beam Epitaxy
MRL	Frederick Seitz Materials Research Laboratory
NW	Nishiyama-Wassermann
PBN	Pyrolytic Boron Nitride
PMMA	Polymethyl Methacrylate
QCM	Quartz Crystal Monitor
RHEED	Reflection High-Energy Electron Diffraction
RIE	Reactive Ion Etch

RRR	Residual Resistance Ratio
STM	Scanning Tunneling Microscopy
TCE	Trichloroethylene
TEM	Transmission Electron Microscopy
UHV	Ultra-High Vacuum
UPS	Ultraviolet Photoelectron Spectroscopy
XPS	X-ray Photoelectron Spectroscopy
XRD	X-ray Diffraction

Chapter 1

Introduction

The present challenge of constructing solid-state quantum bits (qubits) with long coherence times [1] has ignited new interest in Josephson junctions fabricated from single-crystal materials. It has been found that critical-current $1/f$ noise cannot fully account for the observed decoherence times in junctions-based qubits [2]. However, amorphous tunnel-barrier defects can give rise to two-level *charge* fluctuations that destroy quantum coherence across the junction [3, 4]. In an effort to eliminate these defects I sought to fabricate junctions from single-crystal Nb/Al_2O_3 hetero-structures.

Niobium was chosen primarily for two reasons. First, it is a standard material used in the fabrication of Josephson tunnel-junctions [5]. Second, and perhaps more important, is the fact that the epitaxy of niobium on sapphire is well understood [6], and the quality of epitaxial niobium films is extremely high [7]. On the other hand, there have been very few studies of single-crystal Al_2O_3 films grown on refractory metals – only recently was it shown to grow epitaxially on Nb, by both Dietrich *et al.* [8] and myself [9]. At the outset of my thesis work, alumina epitaxy had been studied on a small number materials similar to niobium – tantalum [10], molybdenum [11], and tungsten [12] – but not on niobium itself.

In parallel with my work on epitaxial Nb/Al_2O_3 hetero-structures, Oh *et al.* found that tunnel-junctions from epitaxial $Re/Al_2O_3/Al$ tri-layers had a significantly reduced density of two-level fluctuators [13]. The pairing of rhenium and aluminum oxide had a few advantages over niobium. First is the very small misfit between

the basal planes of rhenium and sapphire ($\sim 0.4\%$). The second advantage is that rhenium is less likely to oxidize, compared with other superconducting refractory metals such as niobium [14]. The disadvantage, however, is that epitaxial Re films develop domains due to basal-plane twinning, causing the surface to be rough on the length scales of a typical tunnel-junction [15].

I report here on my findings concerning the hetero-epitaxy of Al_2O_3 on Nb (110) films. The Al_2O_3 films were grown layer-by-layer with co-deposition of Al and O at elevated substrate temperatures. Epitaxial bi-layers (Nb/Al_2O_3) and tri-layers ($Nb/Al_2O_3/Nb$) were grown on sapphire by molecular beam epitaxy (MBE). The materials were characterized by *in situ* reflection high-energy electron diffraction (RHEED) and x-ray photo-electron spectroscopy (XPS), and *ex situ* atomic force microscopy (AFM), x-ray diffraction (XRD), and electrical transport. Tunnel-junction devices were fabricated from these epitaxial hetero-structures, as well as from epitaxial Nb/Al bi-layers.

In Chapter 2 I survey the experimental methodology, from epitaxial growth and materials analysis to device fabrication and testing. A literature review follows in Chapter 3 with a discussion of Al_2O_3, its various crystal structures and its epitaxy, as well as previous attempts to use epitaxial materials in tunnel-junctions. I begin the discussion of my experimental results in Chapter 4 with the epitaxy of niobium on sapphire. Succeeding that is the analysis of epitaxial aluminum oxide films on niobium (Chapter 5), including device results. In Chapter 6 I discuss the epitaxy of aluminum metal on niobium, as well as the characteristics of tunnel-junctions fabricated from Nb/Al bi-layers. Finally, in Chapter 7, I conclude my thesis with a survey of the potential directions for future research.

Chapter 2

Experimental Methods

2.1 Epitaxial Growth Techniques

For this study, single-crystal films and multi-layers were prepared by means of molecular beam epitaxy (MBE). The MBE chamber was part of a larger ultra-high vacuum (UHV) multi-chamber system in the University of Illinois EpiCenter. In this section I will describe that system, as well as the methods used for growing epitaxial metal and metal-oxide thin films.

2.1.1 Multi-Chamber Growth Facility

The EpiCenter housed a large, multi-chamber UHV system for growing and analyzing single-crystal films and multi-layers. The entire system consisted of six MBE chambers, an XPS chamber and an XRD chamber, all connected by 60 feet of UHV transfer tubes. Each MBE chamber was tailored for a specific material type – the two chambers that I used for my thesis work (systems E and F) were dedicated to refractory metal deposition. A schematic of these chambers is shown in Figure 2.1. The base pressure in the MBE systems was typically 5×10^{-11} torr, while the XPS chamber and transfer tubes were usually at around 10^{-9} torr.

For purposes of MBE, controlled metal evaporation can be achieved either through heating by a resistive filament (effusion cell) or by e-beam bombardment (e-gun). In an effusion cell, the source material sits in a slender crucible whose

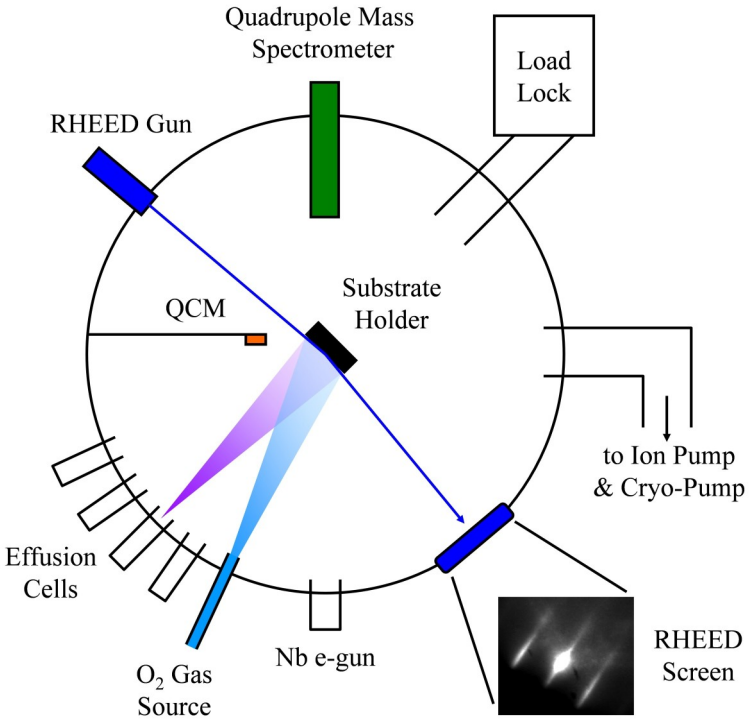

Figure 2.1: EpiCenter MBE Schematic

temperature can be measured and controlled via a thermocouple. Effusion cells can typically operate up to temperatures near 2000 °C. For those materials requiring a higher temperature for evaporation an e-gun may be used. In an e-gun, 10 kV electrons are steered by electromagnets into the source material, which sits in a water-cooled copper hearth. E-guns can reach temperatures of up to 3000 °C and beyond. For the work presented here, an effusion cell was used for aluminum evaporation and an e-gun for niobium. While both systems E and F had e-guns, all the niobium growths were done in system F and aluminum depositions in system E.

For the growth of simple oxides, system E was also equipped with an oxygen gas injector. An ultra-high purity (UHP, 99.995%) O_2 gas bottle was attached to a valve manifold mounted near the chamber. The manifold included a series of on/off and regulating valves that branched off in one direction to a dry roughing pump and, in the other direction, to a precision leak valve mounted on the chamber. The

roughing pump was utilized to reduce the gas pressure behind the leak valve. Inside the vacuum system, a long aspect-ratio tube (12 in $\times$ $\frac{3}{4}$ in diameter) directed the gas flow toward the substrate. With the precision leak valve, the chamber pressure could be controlled at the 10^{-9} torr level – for aluminum oxide deposition, pressures of up to 5×10^{-6} torr were used.

In addition to controlled atomic fluxes, MBE also requires substrate heating and temperature control. In systems E and F, the substrate was heated from the backside by a tantalum filament. The sample temperature could be read out by a thermocouple or, more reliably, by an infrared pyrometer. In both MBE chambers the thermocouple was situated a few millimeters from the substrate backside, resulting in inconsistent temperature readings. Because of this, the more consistent optical method was used instead. The maximum substrate temperature in both systems, E and F, was about 1400 °C.

Other features of the MBE chambers included quartz crystal monitors (QCM) to measure the atomic fluxes. Each system was also equipped with RHEED to monitor the film growth during deposition (see Section 2.2.1 below). Quadrupole mass spectrometers were employed to measure residual gasses and for leak checking. Both chambers utilized liquid nitrogen cryo-panels for cooling and pumping needs.

2.1.2 Substrate Preparation

The substrate material for all of my investigations was sapphire (α-Al_2O_3), with one side polished for epitaxy. The first step in preparing the substrate for growth was the deposition by sputtering of a titanium backside coating, which was necessary for radiative heating. The polished side of the substrate was then scrubbed with cotton swabs dipped in trichloroethylene (TCE) to remove any grease or dirt. Further cleaning was done by sonicating in baths of TCE, acetone, and isopropyl alcohol (IPA) – in that order – for a few minutes each. Finally, the substrate was mounted

on the sample holder and inserted into the load-lock.

Over the course of about four hours, the load-lock was pumped down by a turbo-molecular pump and cryo-pump, in succession. A pressure of about 5×10^{-8} torr was typically reached before moving the sample into the transfer tube and, from there, into the MBE chamber. To further prepare the substrate for epitaxy it was typically outgassed at 600 °C for about 10 hours, followed by a two hour anneal at 1000 °C. From there, the sample was cooled to the appropriate temperature for epitaxial growth.

2.2 Materials Analysis

For the analysis of materials I employed several different techniques. Among these were reflection high-energy electron diffraction (RHEED), x-ray photoelectron spectroscopy (XPS), x-ray diffraction (XRD), and atomic force microscopy (AFM). Electrical transport measurements down to 4 K were also utilized in characterizing films. In this section I give a brief description of each technique, and give examples of what can be learned from each type of analysis.

2.2.1 Reflection High-Energy Electron Diffraction

In RHEED, high-energy electrons (10 kV) are scattered at a grazing angle ($\sim 1°$) off the surface of a substrate or thin film. At this energy, the electron elastic mean free path can vary from 10's to 100's of angstroms, depending on the material. The grazing incidence angle then means that the electrons are scattered from only the first monolayer or two. For this reason, RHEED is very sensitive to the roughness of the film. RHEED is also ideal for monitoring the growth of thin films *in situ* – during deposition or annealing, for example – because of the grazing incidence angle and its non-destructive nature.

For scattering off atomically-flat films, RHEED patterns reveal the reciprocal spatial structure of the two-dimensional surface lattice. For grazing-angle diffraction, the Laue condition is simply $\vec{k}'_{\parallel} = \vec{k}_{\parallel} + \vec{q}$, where $\vec{k}'$ is the outgoing electron momentum, $\vec{k}$ the incoming momentum, and $\vec{q}$ is a reciprocal space vector belonging to the surface lattice of the crystal. Here "$\parallel$" indicates the component parallel to the sample surface. Because the scattering is reduced to two-dimensions, the reciprocal space points can be extended along the surface normal, forming reciprocal space rods. The intersection of these rods with the Ewald sphere is what produces the RHEED pattern.

This assumes that the film surface is actually flat. For rough surfaces, where asperities extend out of the plane, electrons can pass though the crystal. In this case one will sometimes observe transmission or 3D patterns instead of RHEED. Because the electrons pass through the crystal, reciprocal space is no longer populated by rods. Instead, one must consider the full three-dimensional reciprocal space, and the intersection of those points with the Ewald sphere. The contrast between RHEED images and those patterns produced by electron transmission is quite striking. Because RHEED is so sensitive to the nature of the crystal surface it is an ideal *in situ* analysis tool.

2.2.2 X-ray Photoelectron Spectroscopy

XPS – also known as electron spectroscopy for chemical analysis (ESCA) – is a widely used technique for the investigation of solid surface chemistry. Analysis is carried out by irradiating a surface with mono-energetic x-rays and measuring the kinetic energies of emitted electrons. X-ray lines typically used for XPS are Mg-Kα (1253.6 eV) and Al-Kα (1486.6 eV). The emitted electrons are also of two varieties – photoelectrons and Auger electrons. The physical process for each type is shown in Figure 2.2. Photoelectrons absorb the incoming photon energy and are ejected

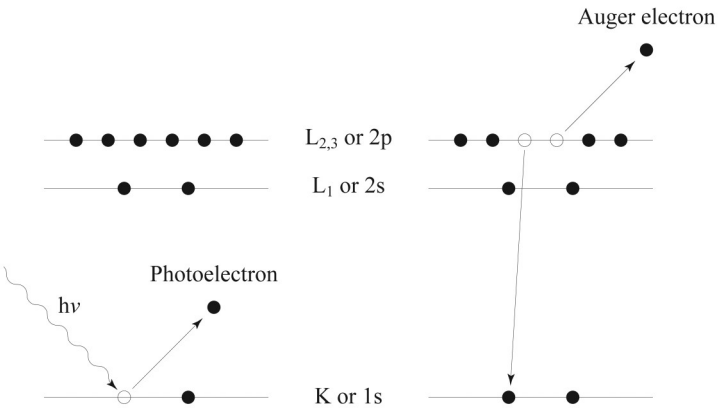

Figure 2.2: The two processes that occur upon x-ray irradiation of a surface. Photoelectrons are ejected from core-level states in the atoms. When an electron from an upper-level decays to fill the vacancy it gives its energy to a neighboring electron. In this secondary process an Auger electron is ejected.

from the atom. The photoelectron's kinetic energy, KE, can be related back to it's binding energy, BE, by the following relation: $\mathrm{BE} = h\nu - \mathrm{KE} - \Phi_s$, where $h\nu$ is the photon energy and Φ_s is the spectrometer work function. Each element has its own unique BE-spectrum, one that can change depending on the atomic valency.

The Auger electron, on the other hand, is emitted due to a secondary process, one where the excess energy of a relaxing outer-electron is given to a neighboring electron. This additional energy can be enough to eject the electron from the atom. Unlike the photoelectron though, the kinetic energy of the Auger electron is insensitive to the energy of the incoming photon. It is for this reason that Auger electron spectroscopy (AES) typically employs incident electrons instead of x-rays. (One can also achieve a much higher incident flux with electrons.) Because of their secondary nature though, the Auger electrons are often neglected during XPS analysis.

The sensitivity of XPS is limited to the near-surface region of the sample. While the photon-induced ionization may occur to depths on the order of a micron, only those electrons emitted near the surface may escape the material without energy loss. This is because the inelastic mean free path of a typical photoelectron is on

the order of 10 Å. So only electrons emitted from the first few tens of angstroms can escape without any energy loss. Those that do lose energy to inelastic scattering but are still emitted simply contribute to the background. The inelastic mean free path depends both on the electron energy and the specific material.

2.2.3 Atomic Force Microscopy

AFM is a type of scanning probe microscope that employs a flexible cantilever with a sharp tip to scan the surface of a sample. Deflection of the cantilever due to sample-tip interaction is measured by reflecting a laser off the cantilever and into a photodiode array. The laser deflection signal is used as feedback to control the sample-tip relative position through a set of piezoelectric crystals. The positioning of the tip relative to the sample is then mapped to the surface topology. The instruments in the Center for Microanalysis of Materials (CMM) can readily achieve sub-nanometer resolution along the surface normal and nanometer resolution laterally.

An AFM can be operated in two basic modes: contact mode and tapping mode. In contact mode, the tip is literally dragged across the sample of the surface and the photodiodes measure a static deflection. In tapping mode, the cantilever is driven near resonance and the tip makes intermittent contact with the surface. In both cases, the piezoelectric crystals control the tip-to-sample distance such that the static deflection (contact mode) or tip amplitude (tapping mode) is constant.

2.2.4 X-ray Diffraction

The XRD instruments employed in this work were the two Philips X'pert systems in the CMM. The standard diffractometer uses Cu Kα x-rays ($\lambda = 1.5406$ Å) and a parallel plate detector to obtain an angular resolution of about 0.03°. The high-

resolution diffractometer uses Cu Kα_1 x-rays and a three-bounce analyzer crystal on the detector to obtain 12 arc-sec resolution ($\sim 0.003^\circ$).

The orientation of the sample in the X'pert systems is shown in Figure 2.3. The incoming x-rays make an angle ω with the surface of the sample. The detector is then placed at an angle 2θ with respect to the incoming x-rays. The sample can be tilted an angle ψ with respect to the x-ray plane, and rotated an angle ϕ about the surface normal. The 2θ and ω goniometers are both high-resolution ($\sim 0.0001^\circ$) while ψ and ϕ have fairly low precision ($\sim 0.01^\circ$).

For fixed angles ψ and ϕ, the XRD instrument can access a semicircular plane of reciprocal space (see Figure 2.3). The semicircle graphically represents the limits of ω (0–90°) and 2θ (ω–180°). The outer radius is where $2\theta = 180^\circ$, or alternatively $\lambda/2d = 1$, where d is the planar spacing in real space. The left and right grayed semicircles represent regions of reciprocal space where $\omega > 90^\circ$ and $\omega < 0^\circ$, respectively.

The work presented in this thesis involves a number of different types of XRD measurements, summarized here:

Radial Scan – Also referred to as a longitudinal or 2θ-ω scan, a radial scan involves varying both 2θ and ω, with ω set to θ minus a constant offset. Such a scan moves along the radius of the semicircular plane in reciprocal space. When the offset is zero, the radius scanned is along the surface normal, and only the specular Bragg peaks are measured. This is the most common measurement performed on thin films. For highly crystalline films, radial scans can show not only reciprocal space points arising from the lattice, but also modulations due to the finite thickness of the film.

Rocking Curve – For a rocking curve or transverse scan, only ω is varied. For this reason, the scan moves along an arc of constant radius, perpendicular to a radial scan. Rocking curves are typically short range scans intended to measure

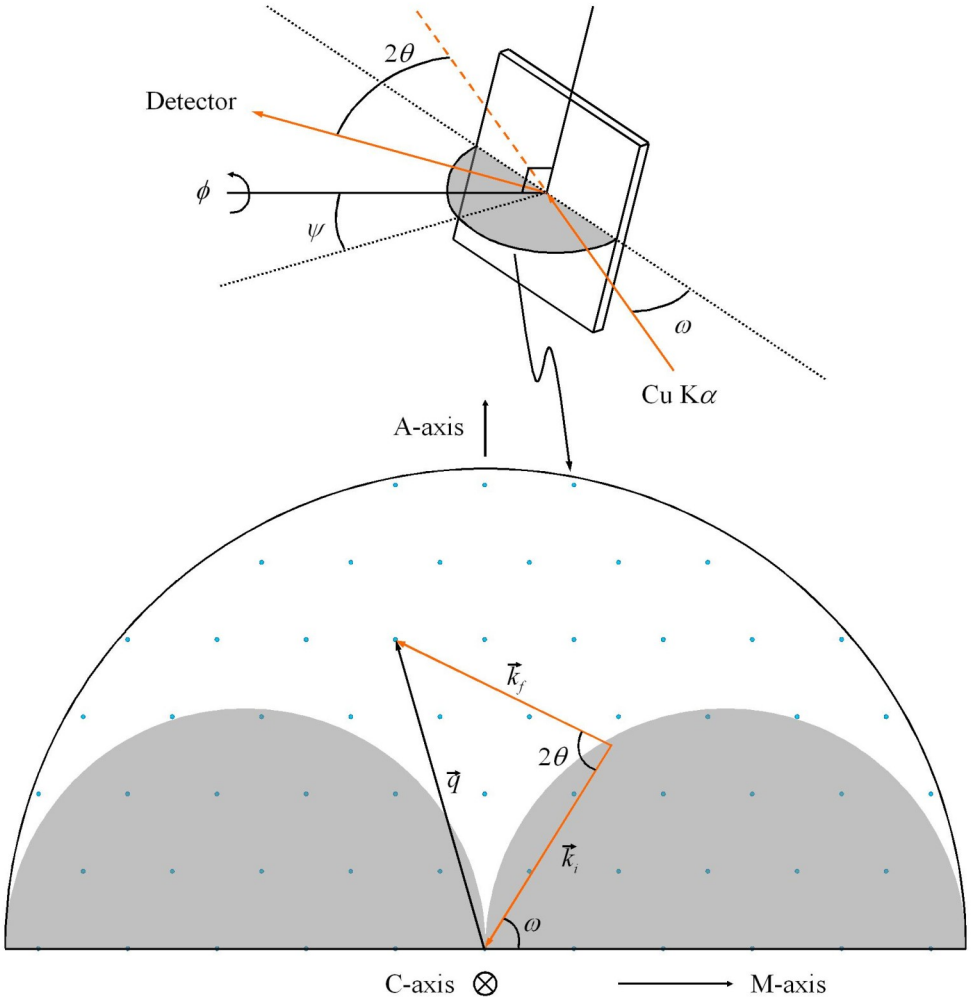

Figure 2.3: Top: Diagram of the XRD setup. Cu Kα x-rays are incident upon the surface at an angle ω with respect to the surface, while the detector is positioned at an angle 2θ with respect to the incoming x-rays. The sample may be tilted an angle ψ and rotated about its normal an angle ϕ. The grayed semicircle indicates the plane in reciprocal space accessible by the instrument. Bottom: As an illustrative example, I show the reciprocal space map for A-plane sapphire, α-Al_2O_3 $(11\bar{2}0)$, along the M-axis azimuth – $[1\bar{1}00]$. The C-axis – [0001] – is perpendicular to the plane, which results in the hexagonal arrangement of lattice points. In the bottom picture the grayed semicircles indicate regions of reciprocal space that are inaccessible due to limitations on the angle ω.

the width of the reciprocal space point of interest. Because they scan the Bragg peaks in a transverse direction, rocking curves are not susceptible to film thickness modulations. The full width at half maximum, $\Delta\omega$ – sometimes referred to as the mosaicity – is often quoted as a measure of structural coherence.

Pole Scan – A pole scan is done by holding 2θ and ω fixed ($\omega = \theta$) and varying ψ and ϕ. ψ is varied from 0–90°, and at each increment ϕ is scanned from 0–360°. The information sought from such a measurement is typically just the in-plane orientation of the film. For a cubic (110) surface, for example, a pole scan with 2θ set to correspond to the (110) Bragg peak will find all the non-specular {110} peaks – (101), (011), $(10\bar{1})$, and $(01\bar{1})$. The *ϕ-Scan* is a subset of the pole scan – variation of ϕ for a single value of ψ.

Reciprocal Space Map – A reciprocal space maps surveys a small area in the semicircular plane shown in Figure 2.3. Often, one is interested in mapping non-specular Bragg peaks, but instead of using the low-precision ψ and ϕ goniometers, only 2θ and ω are varied instead. Reciprocal space maps are a series of radial scans done over a small range of offset angles.

2.2.5 Electrical Transport

The electrical transport properties of epitaxial niobium films were examined using a 4.2 K dipper-probe. The probe allowed for four-terminal resistance vs. temperature measurements. From the traces one could extract the following quantities: the superconducting transition temperature, T_c, the width of the superconducting transition, ΔT_c, the residual resistivity measured at 10 K, $\rho_{10\mathrm{K}}$, and the residual resistance ratio, RRR = $\rho_{295\mathrm{K}}/\rho_{10\mathrm{K}}$, where $\rho_{295\mathrm{K}}$ is the room temperature resistivity. Higher quality films – with fewer impurities and lower densities of crystal defects like dislocations and grain boundaries – will tend to yield larger values for T_c and RRR, and smaller values for $\rho_{10\mathrm{K}}$ and ΔT_c.

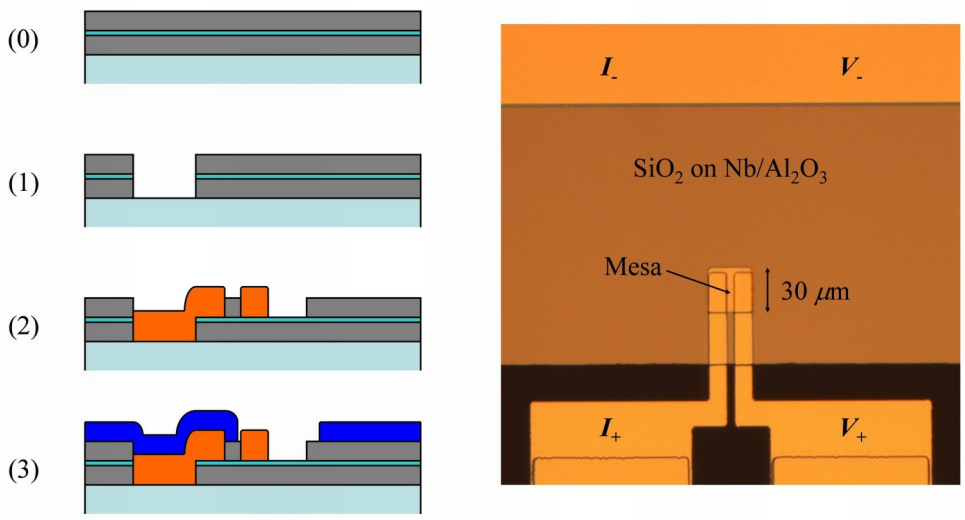

Figure 2.4: The device fabrication process starting with (0) a whole-wafer tri-layer. The steps are (1) device isolation, (2) mesa mill with self-aligned SiO_2 lift-off, and (3) metallization. A picture of a device is shown at right.

2.3 Fabrication and Testing of Tunnel-Junctions

Our ultimate interest was in fabricating high-quality Josephson junctions for their potential use in solid state qubits. In this section I briefly outline the fabrication process, and describe the testing apparatus.

2.3.1 Device Processing

Device fabrication was a three-step process, shown in Figure 2.4, each of which employed standard optical photolithography techniques for defining areas on the sample. Starting with whole-wafer $Nb/Al_2O_3/Nb$ tri-layers, the first step was the device isolation step. The device regions of the sample were electrically isolated from the contact-pad regions by etching through the tri-layer down to the sapphire substrate. The niobium layers were removed with SF_6-based reactive ion etching (RIE), and the alumina barrier was removed by argon ion milling.

The second step was the mesa mill step. Here, the junction area was defined by etching the top niobium away to form a small mesa – 10×10 μm^2 or 30×30 μm^2

– which served as the counter-electrode of the junction. After niobium etching, I used a self-aligned process to lift-off a layer of SiO_2, which served as the wire-up dielectric. The SiO_2 was typically $\gtrsim$ 1000 Å and was deposited by rf sputtering.

Finally, the metallization step was used to make contact to the top and bottom electrodes of the junction. The *in situ* niobium was first milled to remove the native surface oxide – approximately 50 Å was milled – followed by the deposition of an *ex situ* niobium layer by dc sputtering. Contact to the counter-electrode was made through the mesa, while contact to the base-electrode was made through a large area ($\sim$ 10 mm^2) junction.

2.3.2 Device Testing

Devices were tested in a helium transfer-dewar dipper probe designed to operate down to 4.2 K. The temperature was read out using a standard diode thermometer. The current source I used was a custom-built unit that used battery-powered op-amps to convert an ac voltage input to a low-noise current output. This ac voltage was supplied either via a DAQ board or another signal generator at a frequency of 1 Hz. The voltage across the devices was read out using pre-amps and the DAQ board analog inputs that could be sampled at a rate of up to 333 kHz. For the current measurement, the voltage across a 1 Ω series resistor was read out. To further reduce noise effects, 50 Ω series resistors were inserted at the 4.2 K stage on each of the current and voltage leads. Because the custom-built current source had a working range of ± 7 mA, those devices with larger critical currents were tested using a Keithley low-noise current source and nano-voltmeter.

Chapter 3

Literature Review

3.1 Epitaxy of Aluminum Oxide

Over the years, many attempts have been made to grow single-crystal Al_2O_3 films. Alumina has a wide range of uses: as a catalyst for metal particles, as a corrosion-resistant barrier, as an abrasive, and as an insulator in electronic devices. The growth of epitaxial Al_2O_3 has been attempted on a number of different substrates. Because my studies involve the growth of alumina on Nb (110), I will focus my review on similar bcc metals. First, I will discuss the Al_2O_3 crystal structure and the array of different alumina polymorphs. Because each of these polymorphs involves the stacking of close-packed oxygen planes, I will also review the growth of fcc (111) or hcp (0001) on bcc (110) surfaces.

3.1.1 Aluminum Oxide Crystal Structures

Aluminum oxide (Al_2O_3, alumina) is a well-known and well-studied material. It's simple formula, however, veils a complex and variable crystal structure. The thermodynamically stable form of alumina – referred to as sapphire and indicated by the Greek letter α – takes the corundum structure, which can be described by either a rhombohedral or hexagonal crystal lattice. Pauling was the first to describe the sapphire structure in detail [16]. Refinements to the lattice structure were later made by Kronberg [17] and Newnham [18], although Lee and Lagerlof give the most

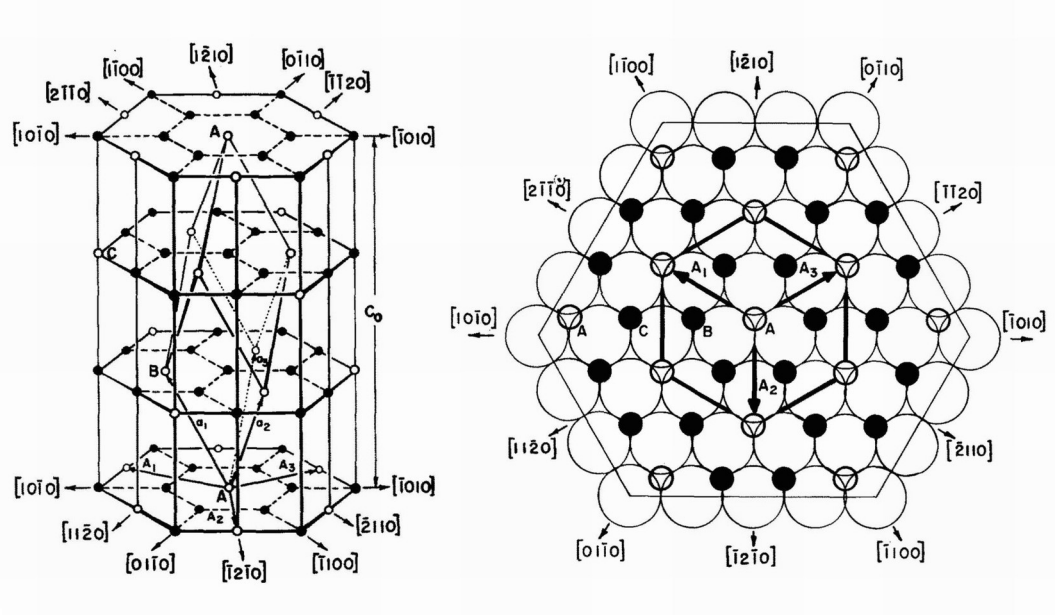

Figure 3.1: The corundum structure of α-Al_2O_3 or sapphire. Left: The aluminum cation sublattice of the morphological unit cell. Open circles indicate the vacant octahedral sites. Note that the structural unit cell has twice the length along the c-axis as the morphological one. Right: The basal plane of sapphire, with both the cation and anion lattices shown. Large circles are used here to indicate oxygen anion positions. Figures taken from Ref. [17].

complete description [19].

The morphological unit cell of the corundum structure is shown in Figure 3.1 (taken from Ref. [17]). Oxygen anions form close-packed planes that are stacked in an hcp arrangement – $ABAB\ldots$ – and the aluminum cations fill 2/3 of the octahedral interstitials. The vacancies left over form an ordered sublattice that defines the unit cell of the crystal. The full stacking sequence is $AC_1BC_2AC_3BC_1AC_2BC_3\ldots$, where the index (1,2,3) indicates the distinct vacancy locations in the Al basal plane. This stacking yields a structural unit cell six layers in height (along the c-axis), twice the height as the morphological unit cell shown in Figure 3.1. The lattice constants for the α-Al_2O_3 structural unit cell at room temperature are $a = 4.7592$ Å and $c = 12.9916$ Å [20].

A number of crystallographic orientations for sapphire are indicated in Fig-

ure 3.1. When employed as a single-crystal substrate for hetero-epitaxy, one of four surfaces is typically used, each of which has come to be identified by letter as often as by Miller indices. The four orientations are: A-plane, $(11\bar{2}0)$; C-plane, (0001); M-plane, $(1\bar{1}00)$; and R-plane, $(1\bar{1}02)$.

In addition to the α form, there exist several metastable or transitional alumina structures. While α-Al_2O_3 has only octahedrally-coordinated aluminum anions (Al^O), the common thread among all the transitional polymorphs is the existence of tetrahedrally-coordinated aluminum anions (Al^T). The various crystal structures can be divided into two broad categories: those with a face-centered cubic (fcc) stacking of close-packed oxygen anions and those with a hexagonal close-packed (hcp) arrangement. Within each category, distinct structures are determined by the distribution of cations. α-Al_2O_3 has a trigonal form with the oxygen planes in an hcp arrangement and with Al^O only. The metastable forms with hcp packing are κ (orthorhombic) and χ (hexagonal). Polymorphs based on fcc packing include γ and η (cubic), θ (monoclinic), and δ (tetragonal). All of these alumina forms are stable at room temperature, with structure transition temperatures ranging from 600-1100 °C [21].

3.1.2 Epitaxy of fcc (111) or hcp (001) on bcc (110)

It has been known for some time that, for the epitaxial growth of an fcc (or hcp) metal on a bcc (110) surface, two in-plane orientations are possible. In almost all cases, fcc metals will grow in the (111) direction, since for bcc metals the (110) surface most resembles close-packing. The in-plane orientation can be of two varieties, depending on the relative size of the atomic radii. One is the Nishiyama–Wassermann relationship (NW), fcc $[1\bar{1}0]$ ∥ bcc [001] [23, 24]. The second is the Kurdjumov–Sachs relationship (KS), fcc $[1\bar{1}0]$ ∥ bcc $[1\bar{1}1]$ or $[\bar{1}11]$ [25]. Both orientations are shown in Figure 3.2 (taken from Ref. [22])

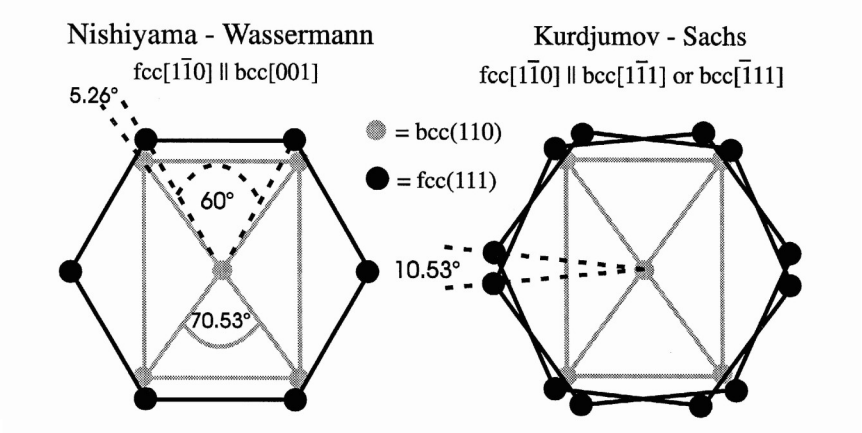

Figure 3.2: For the epitaxy of fcc (111) (or hcp (001)) on bcc (110), two in-plane orientational relationships are preferred: Nishiyama–Wassermann (NW) or Kurdjumov–Sachs (KS). Figure taken from Ref. [22].

A great number of different fcc/bcc metal combinations have been studied over the years, and the orientational relationships observed these metal pairs, with few exceptions, can be predicted based strictly on the ratio of the atomic radii. Rigid-lattice models have been used by a number of authors to determine the energetics associated with different relative orientations of the two lattices [26, 27, 28, 29]. Free-energy minima are observed in these calculations, which indicate the preferred relationship (KS or NW) based strictly on atomic radii ratios.

3.1.3 Al_2O_3 On bcc (110) Metal Surfaces

The first reported growth of epitaxial Al_2O_3 on a bcc (110) surface was done by the Goodman group. They grew ultrathin alumina films on both single-crystal Ta and Mo substrates. Chen *et al.* grew epitaxial Al_2O_3 on Ta (110) substrates by evaporating aluminum metal at a rate of about 0.03 Å/s in an O_2 background of 5×10^{-7} torr at a substrate temperature of 900 K [10]. Both the tantalum surface and the Al_2O_3 films (5–40 Å) were studied with low-energy electron diffraction (LEED). For alumina on Ta (110) a KS relationship was observed, with samples showing either single domain growth or double domain growth. Based on LEED

measurements, it was determined that the alumina was strained about 9% with respect to bulk Al_2O_3. Due to a lack of information regarding the Al sub-lattice, no definitive crystal structure could be determined. The observed crystal lattice was pseudo-hexagonal and showed a 4.2° rotation with respect to the underlying Ta surface.

Following the work on tantalum, Wu *et al.* grew thin Al_2O_3 films on Mo (110) surfaces [11]. The growth method was very different: While the aluminum and oxygen fluxes were roughly equivalent, the substrate was held at room temperature during deposition. The films were then annealed up to 1200 K in the oxygen background to improve the alumina crystallinity. While there is no mention of the orientational relationship, they did use LEED to observe the same pseudo-hexagonal surface lattice that was seen for alumina epitaxy on tantalum. For the films on Mo, Wu *et al.* also used high-resolution electron energy-loss spectroscopy (HREELS) to observe surface optical phonon losses consistent with aluminum oxide thin films. It is also pointed out by Goodman that, due to the substantial misfit between oxide and substrate, strain relief mechanisms for alumina on Mo and Ta are likely to include dislocations and domain-wall structures [30].

Günster *et al.* grew aluminum oxide thin films on W (110) substrates by coadsorbing Al and oxygen [12]. The tungsten substrate was held at 725 K during the deposition. The aluminum flux was such that 13 Å of alumina growth took one hour – roughly 4×10^{-3} Å/s. In other terms, the Al flux was about 0.1 ML/minute, compared with the O_2 flux of 5 L/min (1 L $\approx 1 \times 10^{-6}$ torr-s). Using AES and ultraviolet photoelectron spectroscopy (UPS), they find that the aluminum supplied to the substrate is completely oxidized. For growths done at room temperature, however, they observe both metallic Al and Al^{3+} ions. They also use LEED to observe a pseudo-hexagonal alumina lattice, similar to what was seen for Al_2O_3 epitaxy on Ta (110) [10]. Finally, Günster *et al.* report excellent adhesion between aluminum

oxide films and the W (110) substrate, with the films showing thermal stability up to temperatures around 1200 K.

Dietrich *et al.* recently reported on the growth of epitaxial Al_2O_3 on Nb (110) films [8]. Niobium films were first deposited by sputtering onto a C-plane sapphire substrate at $\sim$ 950 °C, followed by annealing to 1200 °C [31]. The quality of the Nb epitaxy was determined by XRD, scanning tunneling microscopy (STM) and transport measurements. The Al_2O_3 over-layer was formed by evaporating Al at about 0.2 Å/s in an O_2 background of 10^{-6} mbar at room temperature. The film was then annealed 1000 °C in oxygen to achieve crystallization. Oxidation of the aluminum was measured by XPS, and LEED on a 12 Å film showed hexagonal symmetry characteristic of basal plane alumina. However, tunneling microscopy revealed small islands about 4 nm in size, and tunneling spectroscopy found localized defect states at about $\pm$1 eV. No orientational relationship between the niobium and alumina layers was determined.

Finally, Dedkov *et al.* grew crystalline Al_2O_3 layers on the Fe (110) surface by oxidizing ultrathin aluminum films [32]. A 7 Å-thick film was first deposited on the iron surface, showing sharp LEED spots. The metal film was then oxidized by exposing it to 10^5 L at room temperature. Crystallization of the oxide was achieved by annealing at 250 °C for at least 15 min. At this point, LEED images showed a hexagonal surface lattice that was expanded about 4% with respect to bulk sapphire. AES spectra also showed complete oxidation of the aluminum film. The same experiment done with 20 Å-thick Al layers showed no ordered LEED patterns, and AES revealed an incomplete oxidation.

3.2 Epitaxial Hetero-Structures in Tunnel-Junctions

Relatively few attempts at fabricating Josephson tunnel-junctions from epitaxial multi-layers have been reported in the literature. Early experiments aimed simply to duplicate the Gurvitch process [5] using epitaxial Nb/Al bi-layers instead of poly-crystalline ones. More recently, the quest for long coherence times in junction-based qubits has driven a renewed interest in all-epitaxial tri-layers. I review here some of the work that has been done to date.

3.2.1 Tunnel-Barriers from Oxidized Epitaxial Aluminum

Braginski *et al.* were the first to use epitaxial Nb/Al bi-layers in their Josephson junction fabrication process [33]. Nb (110) films were grown on α-Al_2O_3 $(11\bar{2}0)$ substrates by e-beam evaporation at 800 °C. Aluminum was deposited by evaporation at room temperature at a rate of about 0.5 Å/s for a total thickness of 30–50 Å. Diffraction and transport measurements indicated that both layers were of high crystalline quality. Oxidation of the Al surface was done by exposing the bi-layer to 100 mtorr of O_2 for 10–60 min. After oxidation, XPS showed an oxide layer thickness of about 20 Å. For the counter-electrode, PbBi was deposited at room temperature *ex situ*.

Tunnel-junctions fabricated in this manner were characterized by their normal state conductance, G_n, and zero-bias conductance, G_0, and by the ratio $Q = I(4\text{ mV})/I(2\text{ mV})$. While devices fabricated from sputtered, poly-crystalline Nb/Al layers had $Q > 60$, those with epitaxial Nb/Al had $Q = 3$, as shown in Figure 3.3 (from Ref. [33]). Of the four different aluminum morphologies studied by Braginski *et al.*, the epitaxial one showed the poorest device qualities. They infer from their device analysis that the epitaxial Al is nonuniform, and speculate that the high sur-

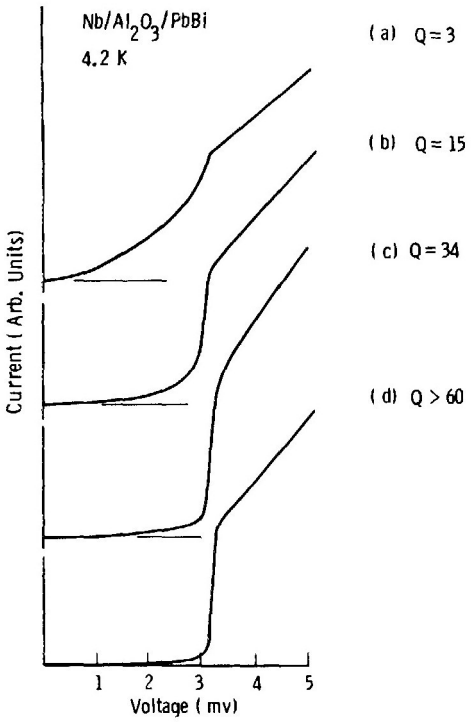

FIG. 1. Quasiparticle tunneling characteristics of four Nb/Al-Al_2O_3/Pb-Bi junctions with thermally oxidized barrier overlayers having different morphologies, $T = 4.2$ K. (a) Highly textured Al evaporated on single-crystal Nb. (b) Barrier of type (a) but amorphized by ion milling. (c) Textured Al sputtered on single-crystal Nb. (d) Untextured, fine-grain Al sputtered on polycrystalline Nb.

Figure 3.3: Dependence of quasi-particle tunneling characteristics on base-electrode growth method. From Braginski *et al.* [33].

face mobility of Al atoms on the clean and crystalline niobium surface may promote island growth in the over-layer. They also suggest that Nb diffusion along oxide grain boundaries might be an additional cause of the observed sub-gap conductances.

Kirk *et al.* followed this work with their own attempt to form tunnel-barriers from epitaxial Al films [34]. Their approach differed from that of Braginski *et al.* in a few ways: First, Kirk *et al.* sputtered their films instead of evaporating. The advantage of sputtering is that the high kinetic energy of the deposited atoms tends to smooth the film and help to form a continuous layer. Second, they employed a liquid nitrogen cooled sample holder to cool the sample during Al growth, reducing

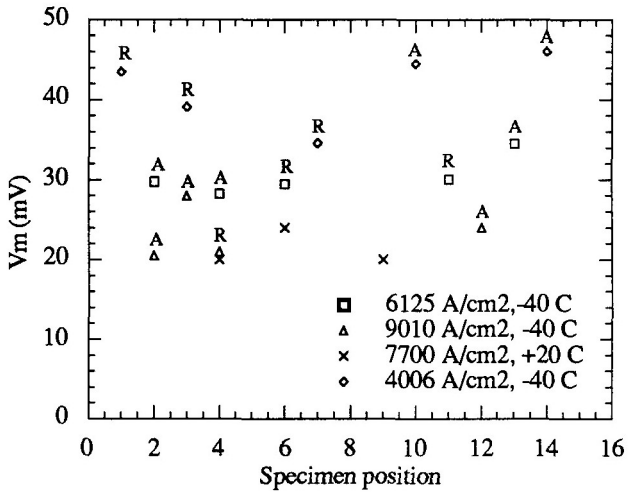

Fig.4. Mean V_m values from each sspecimen from the three runs with Al deposited at -40°C and the run with Al deposited at 20 °C, plotted against position on heater/cooler during the deposition run. The -40°C substrates are identified as A- orR-plane.

Figure 3.4: Dependence of V_m on growth conditions and substrate choice. From Kirk *et al.* [34].

the aluminum mobility on the niobium surface and, with it, the possibility of island nucleation. Finally, two different sapphire substrate orientations were used for their samples – A-plane and R-plane. Niobium grew epitaxially on both surfaces at about 750 °C. However, aluminum grew epitaxially only on those samples with A-plane substrates. Al metal was deposited at a rate of about 0.3 Å/s for a total thickness of 40–50 Å, with the substrate temperature at either +20 or -40 °C. Crystallinity of the films was measured by x-ray diffraction. The tunnel barrier was formed by oxidizing the Al at an O_2 pressure of about 40 mtorr for 10 min. Finally, the counter-electrode was sputtered – first a thin Al capping layer, then Nb.

Kirk *et al.* used two parameters to characterize their tunnel-junctions: the critical current density, J_c, and the standard quantity $V_m = I_c R_{sg}$, where I_c is the critical current and R_{sg} is the sub-gap resistance, typically measured at 2 mV for niobium-

based devices. For their devices, J_c ranged from 4000–9000 A/cm^2 and V_m varied between 20 and 50 mV at 4.2 K. Generally speaking, those devices with a higher J_c also had a lower V_m. Two other trends were also apparent: First, lower aluminum deposition temperatures yielded higher quality junctions. Second, comparing the qualities of devices on A-plane and R-plane sapphire showed no obvious advantage for epitaxial Al. These findings are summarized by the data shown in Figure 3.4.

3.2.2 Tunnel-Barriers from Epitaxial Aluminum Oxide

Recently Oh *et al.* demonstrated the feasibility of epitaxial Al_2O_3 films as tunnel-barriers for Josephson junctions [35]. As a base-electrode they used rhenium, which grows on C-plane sapphire in the (0001) orientation at 850 °C. Rhenium is well lattice-matched with basal-plane sapphire ($\sim 0.4\%$ misfit) and has a superconducting critical temperature around 2 K. Aluminum metal was evaporated at room temperature onto the Re (0001) surface at a rate of about 0.03 Å/s in an O_2 background of 1×10^{-6} torr. This served to form an amorphous AlO_x layer about 20 Å thick. Single-crystal Al_2O_3 was then formed by annealing the oxide film to 800 °C in 4×10^{-6} torr of O_2 gas. The counter-electrode employed in these tri-layers is sputtered poly-crystalline Al. The epitaxy of the base Re layer and the alumina barrier were verified with RHEED.

Current-voltage (I–V) characteristics for tunnel-junctions fabricated from epitaxial Re/Al_2O_3-based hetero-structures were measured at 80 mK. (See Figure 3.5) Devices were also characterized by a quality factor, Q, similar to that used by Braginski *et al.* [33]. Because of their use of different metals for the base- and counter-electrodes however, Oh *et al.* used the definition $Q = I(0.70\text{ mV})/I(0.35\text{ mV})$ and found a value of 1200 for their devices. When implemented into a qubit architecture, these epitaxial barriers also showed a reduced density of two-level fluctuators, when compared with conventional junctions with amorphous AlO_x barriers [13]. This

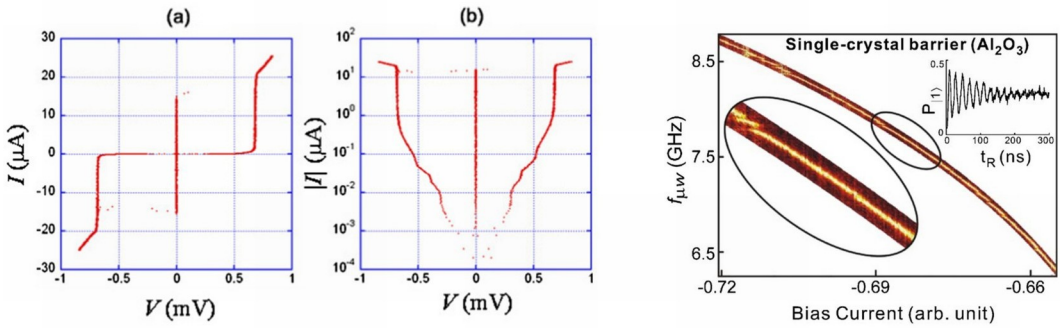

Figure 3.5: Left: I-V characteristics of a tunnel-junction employing epitaxial Re/Al_2O_3 layers plotted on both linear (a) and logarithmic (b) scales. (From Ref. [35]) Right: Spectroscopy scan for a qubit utilizing epitaxial Re/Al_2O_3 showing a reduced number of two-level fluctuators. (From Ref. [13])

finding, demonstrated by the qubit spectra shown in Figure 3.5, confirmed the view that many had [3, 4]: that defects in the tunnel-barrier were largely responsible for the observed decoherence in qubits.

It is clear from the literature that neither the epitaxy of aluminum oxide nor the use of epitaxial alumina films in Josephson junctions has received much attention. I believe that this is changing now due to the interest in solid state qubits. While the devices fabricated from epitaxial Re/Al_2O_3 layers are promising, developing our knowledge of alumina hetero-epitaxy is an important step toward understanding their impact in tunnel-junction-based quantum bits.

Chapter 4

Epitaxial Niobium on Sapphire

The hetero-epitaxy of niobium on sapphire has been well studied over the past few decades, as evidenced by the recent review by Wildes *et al.* [36]. In this chapter I discuss my own findings regarding niobium epitaxy on sapphire, with references to related original literature where appropriate. Before that, I discuss a unique aspect of the Nb-Al_2O_3 system: the three-dimensional growth relationship.

4.1 Three-Dimensional Relationship for Nb on α-Al_2O_3

The first experiments involving the hetero-epitaxy of niobium on sapphire were geared toward the growth of Nb-Cu [37] and Nb-Ta [38] superlattices. In both cases, A-plane sapphire – α-Al_2O_3 $(11\bar{2}0)$ – was used as the substrate, yielding Nb (110) base layers. However, Durbin *et al.* demonstrated that epitaxial Nb-Ta superlattices could be formed on a number of common sapphire orientations [6]. Their findings revealed a three-dimensional relationship between the α-Al_2O_3 substrate and the Nb over-layer:

$$Al_2O_3\ [11\bar{2}0] \parallel Nb\ [110] \text{ and } Al_2O_3\ [0001] \parallel Nb\ [\bar{1}11]$$

This relationship is illustrated in Figure 4.1 (taken from Ref. [36]). While Durbin's discovery was achieved via XRD studies, later reports involving RHEED [39], and

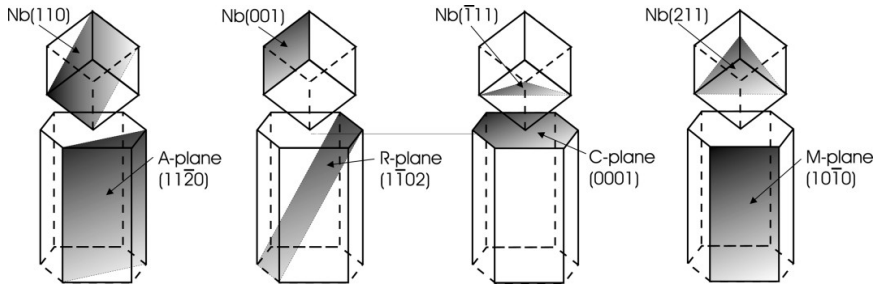

Figure 4.1: The three-dimensional relationship governing the epitaxy of niobium on sapphire, with the four most common substrate orientations shown. Figure taken from Ref. [36].

electron microscopy [40] confirmed this unique relationship between Nb and α-Al_2O_3.

Using high-resolution transmission electron microscopy (HRTEM) to image the Nb/sapphire interface, Gutekunst *et al.* developed a building principle to explain the origins of this 3D relationship [41]. On the oxygen-terminated sapphire surface, they argue, niobium atoms in the first monolayer arrange themselves so as to continue the Al sublattice across the interface. The atoms in the second niobium layer are not so strictly bound to Al sublattice positions, but even their positions approximate Al ones. This building principle can be attributed to overall similarities between the Nb unit cell and the Al sublattice in α-Al_2O_3. It also explains why twinned films have never been observed in the Nb/sapphire system.

However, there is one exception to the three-dimensional relationship that has been found. Under some conditions, Nb (110) will grow on C-plane sapphire with domains oriented in three different in-plane orientations: Nb [001] $\parallel$ α-Al_2O_3 [$\bar{1}$100], [0$\bar{1}$10] and [10$\bar{1}$0]. These domains are situated at 120° with respect to each other, reproducing the hexagonal symmetry of the Al_2O_3 substrate. This type of film structure has been observed only under the following conditions: evaporation above 1000 °C [42], post-growth annealing up to 1500 °C [43], and niobium sputtering near 850 °C [31].

4.2 Nb Epitaxy on A-plane Sapphire

4.2.1 Growth and Annealing Procedures

The niobium films employed for the subsequent growth of aluminum oxide were all deposited in System F at a substrate temperature in the range 750–800 °C. High-purity Nb (99.99%) was evaporated at a rate of 0.3–0.5 Å/s. The chamber base pressure – with the substrate at growth temperature and the liquid nitrogen shrouds cold – was typically in the mid-10^{-11} torr range. With the niobium e-gun source hot enough for evaporation, the chamber pressure was usually in the upper-10^{-9} torr range. Nb layers used for Al_2O_3 epitaxy were either 1000 or 2000 Å thick.

RHEED measurements of the as-grown Nb (110) surface showed well-defined 1st-order streaks and Kikuchi lines. The specular spot was typically elongated to some degree in the vertical direction, indicating a surface fluctuation of a few hundred nanometers lateral size. Figure 4.2 shows images from RHEED along the $[\bar{1}11]$, $[1\bar{1}1]$, and [001] azimuths. Diffraction patterns along the $[\bar{1}11]$ azimuth would usually show 1/3-order streaks, while similar intermediate streaks were very faint along the $[1\bar{1}1]$ direction, if visible at all. 1/2-order streaks were typically observed along the [001] and $[\bar{1}10]$ direction.

These RHEED patterns were recognized by Sürgers and Löhneysen as arising from a reconstruction due to the surface segregation or adsorption of oxygen during film growth [44]. The surface lattice structure they derived from such a reconstruction is shown in Figure 4.2. They also found that the only procedure to lift the reconstruction was to grow at temperatures below 450 °C, where epitaxy led to island growth. Haas *et al.* had earlier used LEED to observe the same surface reconstruction on clean Nb (110) crystals exposed to small doses of O_2 at room temperature [45].

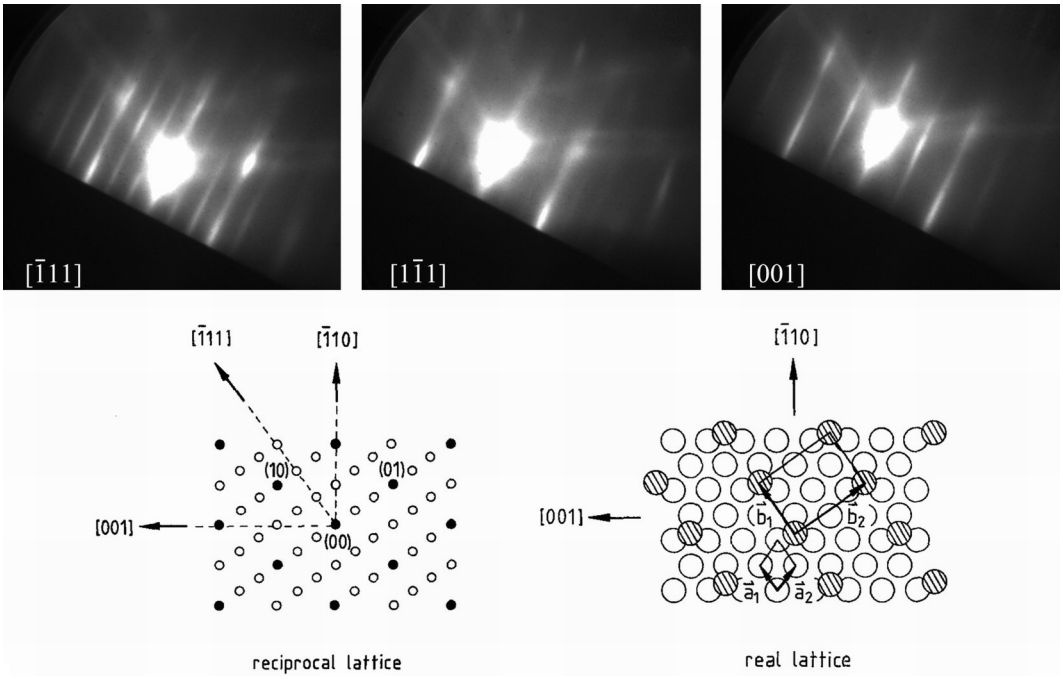

Figure 4.2: RHEED images and surface lattices for as-grown Nb (110) on sapphire. The reconstruction seen in the RHEED patterns is due to surface segregation or adsorption of oxygen during growth. The corresponding reciprocal and real space lattices are shown in the bottom diagrams, both of which were taken from Ref. [44].

Many of the niobium films that I grew were also annealed immediately after deposition and RHEED measurements were performed. Annealing took place at temperatures ranging from 1300–1370 °C for a duration of one hour. The substrate temperature was ramped up from growth temperature over the course of 15 min. After annealing, the substrate heater power was turned off over a period of 2 min and the sample was allowed to cool. During the annealing procedure, the chamber pressure typically peaked at about 10^{-9} torr at the end of the annealing period. With the substrate at these high temperatures, the residual gases in the chamber were predominantly nitrogen and carbon dioxide.

Annealed Nb (110) films showed RHEED patterns that were strikingly different from those viewed after deposition. Nowhere was this more evident than for RHEED along the [$\bar{1}$11] azimuth, as seen in the diffraction pattern in Figure 4.3. Before

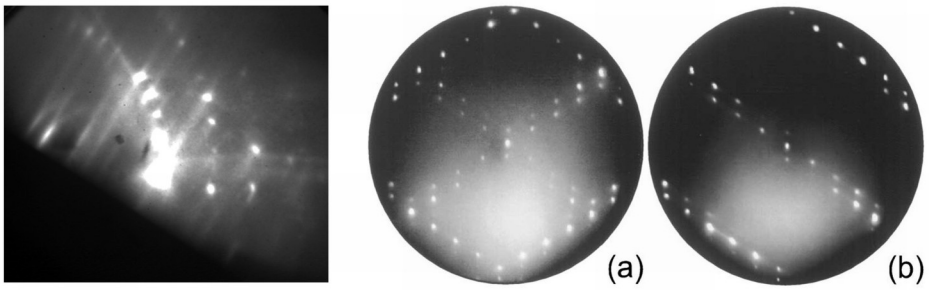

Figure 4.3: On the left is RHEED along the [$\bar{1}$11] azimuth for an annealed Nb (110) film. The asymmetric rings replicate what has been observed by LEED imaging – data from Ondrecjek *et al.* [46] is shown on the right. While the LEED work revealed two variants, in my films I typically observe only one.

annealing, RHEED showed 1/3-order streaks for this orientation. After annealing however, the diffraction pattern showed 1/4-order streaks with asymmetric spot-rings clearly visible. It should be noted that this RHEED pattern was never observed along the [1$\bar{1}$1] azimuth.

The observed diffraction images agreed well with LEED results obtained by a number of authors. Pantel *et al.* found this surface reconstruction by exposing niobium single-crystals to small doses of oxygen gas ($\sim$ 20 L) at room temperature [47]. Crystallization of the surface was achieved by annealing, and they found the reconstruction stable up to temperatures of 1500 °C. Ondrecjek *et al.* also observed these LEED patterns for Nb (110) thin films and bulk crystals annealed in UHV [46]. Using an Auger surface probe, they noted that the reconstruction was due to uncontrolled O adsorption over time; and whereas I saw only one variant in RHEED, both Pantel *et al.* [47] and Ondrejcek *et al.* [46] observe two variants of the surface reconstruction. (See Fig. 4.3.) I speculate that this is due to vastly different thermal treatments. For the LEED investigations, Ondrejcek *et al.* cycled their samples above 1700 K numerous times in an attempt to relax the crystal lattices.

Arfaoui *et al.* have also observed these same LEED patterns for annealed Nb (110) crystals [48, 49]. For their work, they annealed niobium single-crystals in

UHV to temperatures between 1500–2000 K. They used XPS and STM measurements to argue that the Nb (110) surface is tiled with $NbO_{x\approx1}$ nanocrystals upon annealing. NbO takes the NaCl structure – interlaced fcc lattices with basis vectors $b_{Na} = (0,0,0)$ and $b_{Cl} = (\frac{1}{2},\frac{1}{2},\frac{1}{2})$ – except in NbO both the (0,0,0) and $(\frac{1}{2},\frac{1}{2},\frac{1}{2})$ atoms are absent. Arfaoui *et al.* find that these $NbO_{x\approx1}$ nanocrystals assume a KS orientational relationship with NbO (111) ∥ Nb (110) and an in-plane orientation NbO $[1\bar{1}0]$ ∥ Nb $[\bar{1}11]$.

4.2.2 Determination of Optimal Growth Parameters

For the epitaxy of metals, Flynn found a general rule concerning the optimal growth temperature [50]. Citing the common characteristics of most metals, he arrived at approximate expressions for both the bulk diffusion, $D_b(T)$, and surface diffusion, $D_s(T)$, as a function of temperature:

$$D_b(T) \simeq 10^{-1/2}10^{-7T_m/T}\ \mathrm{cm}^2/\mathrm{s}$$
$$D_s(T) \simeq 10^{-3}10^{-3T_m/2T}\ \mathrm{cm}^2/\mathrm{s}$$

To limit bulk diffusion, one should deposit at lower substrate temperatures, while higher temperatures are called for to increase surface diffusion. Using reasonable assumptions for other growth parameters – the atomic flux rate and growth duration, for example – Flynn arrived at an upper limit for D_b (10^{-19} cm^2/s) and a lower limit for D_s (10^{-7} cm^2/s). These two limits suggest a narrow temperature range for ideal metal epitaxy at $T \sim 3T_m/8$. For niobium ($T_m \approx 2480$°C) this points toward a growth temperature of about 760 °C.

While Flynn's "3/8-rule" provided a good starting point, it was necessary to find the appropriate growth parameters to yield the type of Nb films needed for tunnel-junction devices. The most important aspect of the niobium film was its flatness – a rough surface would lead to a poorly defined interface between the niobium and

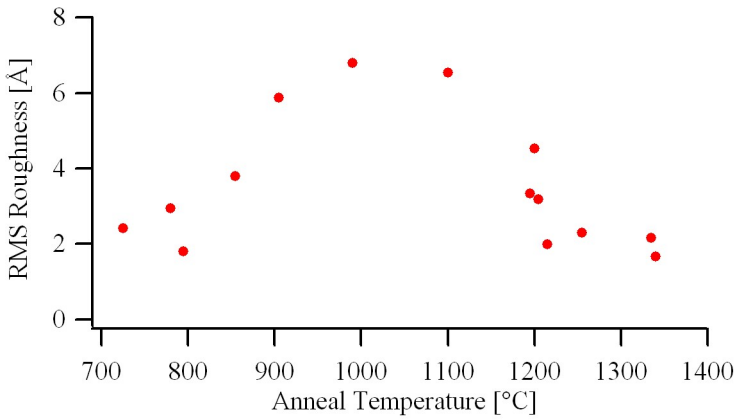

Figure 4.4: The rms roughness of Nb (110) films grown on A-plane sapphire as a function of annealing temperature, as determined by *ex situ* AFM. Films grown around 750–800 °C have roughnesses approaching 2 Å rms. Intermediate annealing temperatures results in faceting and step-edge bunching, while high temperature annealing produces wide terraces with parallel monatomic step-edges. The films used for this figure ranged in thickness from 1000–3000 Å.

any kind of over-layer. To determine the optimum growth procedure for yielding atomically-flat films I grew several Nb films at temperatures ranging from 750–950 °C. Some films were then annealed up to temperatures exceeding 1300 °C. *Ex situ* AFM was used to determine the rms roughness of the niobium surface, and in Figure 4.4 I plot the measured film roughness versus the film annealing temperature.

Figure 4.4 should not be construed as representing the complete set of niobium films grown. Quite the opposite, most films showed significantly higher roughness than what is presented. Rather, Figure 4.4 was the standard by which all niobium films were judged. Rougher films were often viewed as an indication of contamination, either in the chamber – a vacuum leak, for example – or in the source material – contamination or oxidation, for example. Once films with sufficient flatness could be grown, then the niobium was ready for subsequent aluminum oxide hetero-epitaxy.

In Figure 4.5 I show AFM images for three different annealing temperatures. For films grown at temperatures around 750–800 °C and not annealed, the surface shows height fluctuations that span distances of several hundred nanometers – a sort of

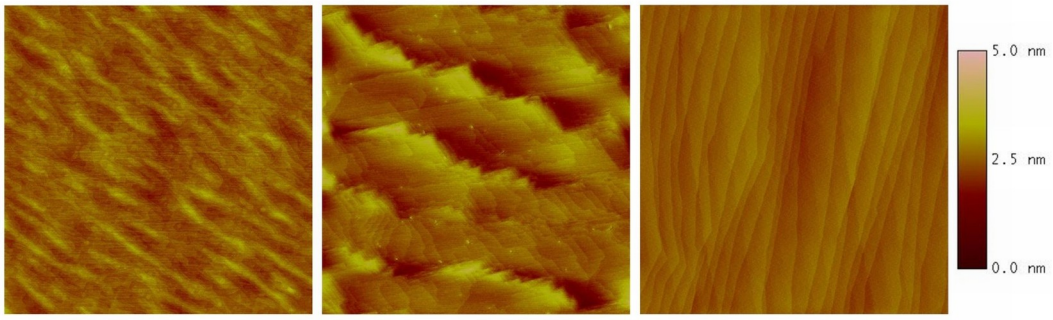

Figure 4.5: AFM images from Nb (110) films after various stages of annealing. At left is an unannealed film grown at 780 °C. The middle image is from a film annealed to 990 °C, while the rightmost film was annealed to 1255 °C. All images are 5 μm $\times$ 5 μm, with the height scale shown at right.

"rolling hills" landscape. The rms roughness of an unannealed film was as small as 2 Å. Films annealed at intermediate temperatures (900–1100 °C) show facets and step-edge bunching. The highest annealed films show large terraces and roughly parallel mono-layer step-edges about 2 Å in height. This agrees well with Nb (110) planar spacing – $a/\sqrt{2} = 2.338$ Å. For samples annealed above 1250 °C, faceting is minimized as the step-edges align according to the substrate miscut. Surface roughness is typically less than 2 Å rms.

Flynn *et al.* have observed such surfaces in annealed films previously using low-energy electron microscopy (LEEM) [51, 52]. They showed that, due to the low energy nature of bcc {110} surfaces the facets developed during moderate-temperature anneals ran perpendicular to off-axis ⟨110⟩ directions. At higher temperatures, they saw these facets dissipate into parallel monatomic step-edges. It was these atomically-smooth niobium surfaces that I sought for the hetero-epitaxy of Al_2O_3.

4.2.3 Further Analysis of Nb (110) Thin Films

Although the growth of niobium was geared toward providing atomically flat surfaces on which to grow aluminum oxide, the crystalline qualities of our films were also measured by means other than RHEED and AFM. XRD measurements on niobium

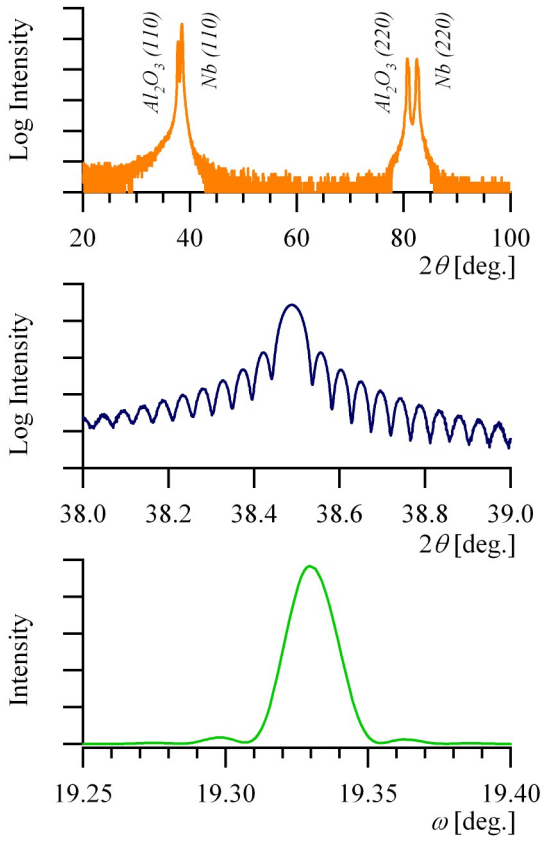

Figure 4.6: XRD scans for a 2000 Å thick Nb (110) film on A-plane sapphire. Top: Radial scan of specular Bragg peaks showed the single-crystal nature of the film and substrate. Middle: Close-up view of Nb (110) Bragg peak, with film-thickness oscillations indicating the structural coherence of the film. Bottom: Nb (110) rocking curve, with a narrow peak indicative of high-quality epitaxy.

(110) films confirmed their single-crystal nature. As shown in Figure 4.6, radial scans showed only the Nb (110) and α-Al_2O_3 $(11\bar{2}0)$ Bragg peaks. Intensity fringes in the Nb (110) peak indicated a sharp interface and surface as well as a structural coherence that extended over the entire film thickness. Rocking curves typically had a FWHM of about 0.03°.

The in-plane orientation of the niobium film with respect to the sapphire substrate could be determined in a number of ways. RHEED evidence alone showed the alignment of the Nb $[\bar{1}11]$ and α-Al_2O_3 [0001] directions. XRD pole scans for both substrate and film peaks could also be done. A more elegant picture, however,

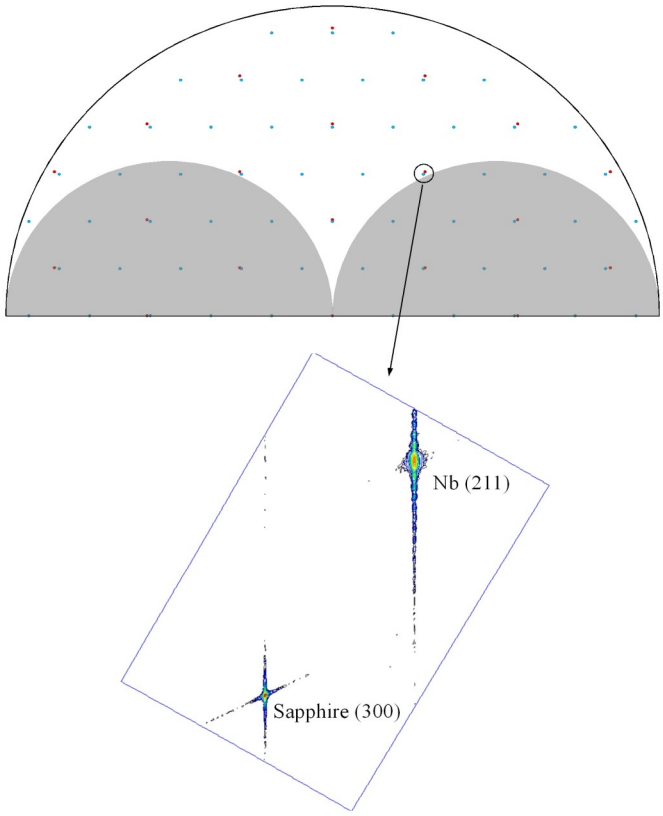

Figure 4.7: A reciprocal space map of niobium on A-plane sapphire. The top image shows the expected locations of all points in the instrument-accessible reciprocal space with α-Al_2O_3 [$1\bar{1}00$] in the x-ray plane. The bottom picture shows the mapping of the Nb (211) and α-Al_2O_3 ($30\bar{3}0$) Bragg peaks.

is a reciprocal space map. For Nb (110) on A-plane sapphire, not only is Nb [$\bar{1}11$] $\parallel$ α-Al_2O_3 [0001], but also Nb [$\bar{1}1\bar{2}$] $\parallel$ α-Al_2O_3 [$1\bar{1}00$], consistent with the three-dimensional relationship described above and shown in Figure 4.1. This in-plane alignment places the Nb (211) and sapphire ($30\bar{3}0$) Bragg peaks very near to one another in reciprocal space. Figure 4.7 shows a map of reciprocal space near these two points. The mapping agrees very well with the expected positions of the two Bragg peaks. In addition, the finite-thickness fringes that appeared in the radial scan of the Nb (110) peak (Fig. 4.6) were also clearly visible in the Nb (211) peak.

The Nb (211) peak, and other off-specular Bragg peaks, were also used to determine the strain of the niobium films. In Table 4.1 I show results from the measure-

Nb Thickness (Å)	Bragg Peak	2θ	d (Å)	a (Å)
1000 (A)	(220)	82.6540°	1.16646	3.29925
	(310)	95.1606°	1.04342	3.29960
	(400)	138.0509°	0.82494	3.29976
	(211)	69.7461°	1.34721	3.29997
	(222)	107.9052°	0.95269	3.30022
	(321)	121.7153°	0.88192	3.29984
2000 (A)	(220)	82.4511°	1.16882	3.30592
	(310)	94.9791°	1.04494	3.30439
	(400)	137.6734°	0.82599	3.30396
	(211)	69.6461°	1.34890	3.30412
1000 (U)	(220)	82.7681°	1.16517	3.29561
	(400)	137.5701°	0.82630	3.30520
	(321)	121.4918°	0.88290	3.30353
	(222)	107.7068°	0.95392	3.30447

Table 4.1: Determination of the lattice strain for Nb (110) films grown on A-plane sapphire, both annealed (A) and unannealed (U). Using the measured 2θ values, both the planar spacing, d, and lattice constant, a, were determined. Compared with bulk niobium ($a = 3.3066$ Å) the 1000 Å film is strained about 0.2% while the 2000 Å film shows only 0.06% strain. The unannealed film shows an out-of-plane compressive strain and an in-plane tensile strain, both at about the 0.3% level.

ment of strain in three films – a 1000 Å film and a 2000 Å one, both annealed to about 1340 °C, and an unannealed 1000 Å film. In addition to the specular (220) peak, several off-specular peaks were measured using the high-resolution diffractometer ($\Delta\theta \approx 0.003°$). The measurements show that, on average, the annealed 1000 Å film is strained about 0.2% while the 2000 Å film shows only 0.06% strain. The unannealed film shows compressive strain of about 0.3% along the [110] direction, and tensile strain at about the same level in the plane of the film.

Transport measurements were also routinely performed, both on whole sample films and on fabricated devices. Early experiments on 3000 Å niobium films showed that films grown near 800 °C had RRR above 100 and T_c above 9.4 K. (See Figure 4.8.) Residual resistivity, ρ_{10K}, approached 0.1 $\mu\Omega$-cm. These values are comparable with other reports of transport properties in epitaxial Nb films [53, 54]. Annealed niobium films typically showed a higher residual resistivity and lower T_c and RRR

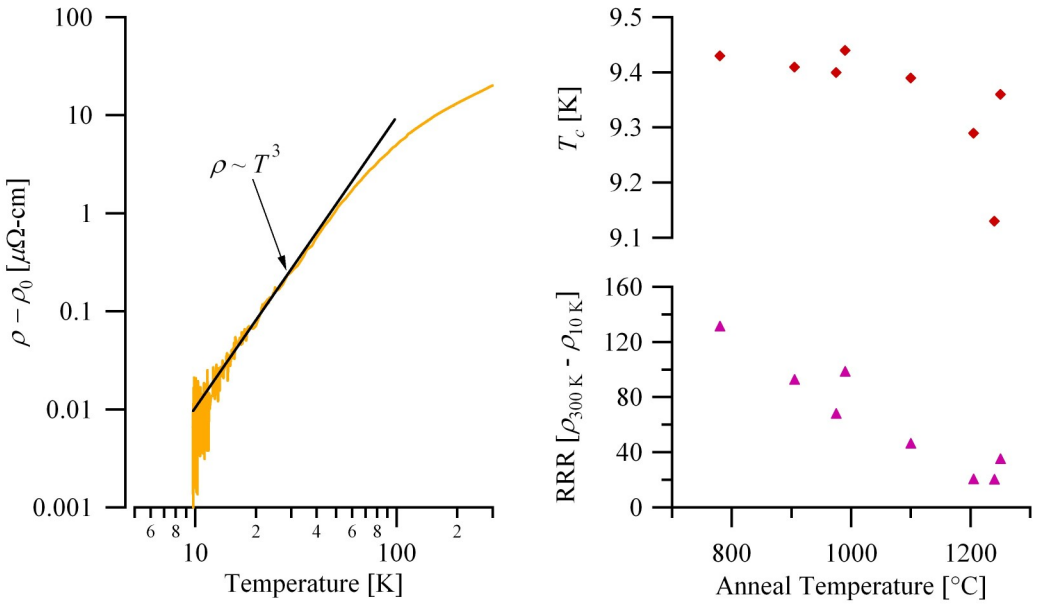

Figure 4.8: Left: A plot of the resistivity of a 3000 Å Nb film on A-plane sapphire. The observed T^3 behavior between 10 K and about 50 K agrees well with earlier work by Webb [56] using large-RRR bulk niobium crystals. Right: RRR and T_c for several 3000 Å films plotted versus annealing temperature. Reduction of both quantities at higher temperatures is likely due to oxygen adsorption.

than unannealed ones. Knowing that annealing leads to improved structural and morphological properties, this seems counterintuitive. The most likely explanation was an increased concentration of oxygen in the bulk of the film. I have already discussed how oxygen transforms the Nb (110) surface upon annealing (see Section 4.2.1). In 1963 De Sorbo found that a small amount of oxygen dissolved in bulk niobium can have substantial effects on its transport properties [55]. Specifically, he found that below the solubility limit for oxygen in niobium ($\sim$ 3.83 at.%) T_c decreased and ρ_{10K} increased approximately linearly with oxygen percentage – 0.93 K/at.% and 5.2 $\mu\Omega$-cm/at.%, respectively. For my films this translates to about 0.3 at.% O_2 adsorbed over the temperature range 780–1250 °C.

The resistivity of 3000 Å Nb (110) films at low temperatures shows power-law behavior, as seen in Figure 4.8. Between 10 K and about 50 K, the resistivity goes like T^3. This result agrees with the earlier work of Webb [56]. Using bulk crystals

with RRR greater than 10^4 he observed the same T^3 behavior.

4.3 Summary

For the subsequent hetero-epitaxy of aluminum oxide thin films I sought a flat Nb (110) surface on which to grow. I found that both annealed and unannealed niobium films had an optimum rms roughnesses of about 2 Å or less. The transport characteristics were also found to vary with temperature, which is likely due to the adsorption of oxygen. Diffraction measurements were also performed on the niobium films – *in situ* RHEED imaging of the surface reconstruction agreed well with what has been reported in the literature, and XRD confirmed the single-crystal nature of the film, showing narrow line widths and low levels of residual strain. These low strain values are important because they support the use of niobium RHEED patterns to calibrate the RHEED system. With a calibrated RHEED system it becomes possible to determine the surface lattice spacing of a film *in situ*. This is precisely what I did for thin Al_2O_3 films grown on Nb (110) surfaces, the topic of the succeeding chapter.

Chapter 5

Epitaxial Aluminum Oxide on Niobium Thin Films

I have studied the hetero-epitaxy of Al_2O_3 on both annealed and unannealed Nb (110) films. Because of the differing surface reconstructions, the procedures for alumina growth were slightly different for the two cases. In this chapter I discuss the growth of aluminum oxide on both surfaces, and show current-voltage characteristics for tunnel-junctions fabricated from both.

5.1 Al_2O_3 Hetero-Epitaxy on Annealed Nb (110)

5.1.1 Growth Procedures

As was mentioned in Chapter 2, the niobium films for samples described in this thesis were all grown in System F, while alumina films were grown in System E. After Nb deposition, the samples were allowed to cool to below 200 °C before transferring them from F to E. The transfer took only a few minutes, limiting the exposure of the niobium surface to residual gases in the tube. Once in System E, the substrate was warmed back up to growth temperature. RHEED measurements on the niobium surface showed no changes from those done in System F.

For annealed Nb (110) surfaces, the Al_2O_3 was typically deposited at a substrate temperature near 800 °C. Aluminum metal (99.9995%) was evaporated at about 0.1 Å/s, which required a cell temperature of 1020 °C. With the Al cell at growth temperature, and with a mask covering the substrate, the Al shutter was opened.

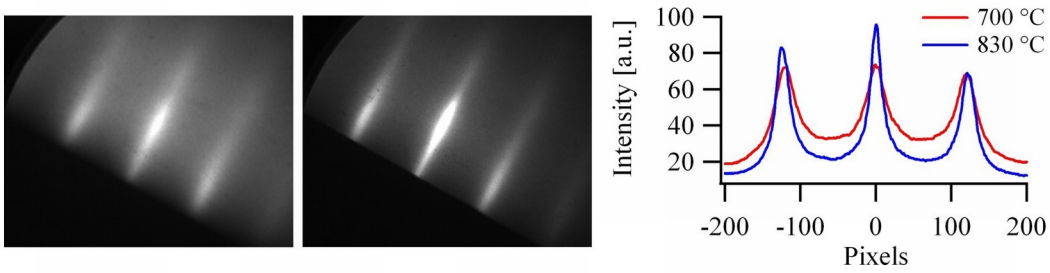

Figure 5.1: A comparison of RHEED from Al_2O_3 films grown on annealed Nb (110) at 700 °C (left) and 830°C (right). Both the streak width and the diffuse background show improved crystallinity at the higher temperature. To further illustrate the comparison, line-scans of both images are shown in the graph at right.

At this point the Al flux was measured with the QCM. The chamber pressure with the Al source on was typically 1×10^{-9} torr. At this point, ultra-high purity O_2 (99.995%) was bled into the chamber through the precision leak valve and injector tube, bringing the chamber pressure up to $0.5–5\times10^{-6}$ torr. At the lower end of this pressure range I estimate that the O_2 flux is about 1000 times greater than that of Al.[57] Deposition began when the substrate mask was removed to expose the sample.

The alumina growth was stopped by closing the Al shutter. However, a variety of different oxidation treatments were attempted to ensure proper stoichiometry in the film. In the simplest case, the O_2 flux was left on for 5 min while the sample sat at the growth temperature. For the most extensive oxygen dosage, in addition to the 5 min at growth temperature the sample was also cooled to 200 °C over 30 min before the O_2 was turned off. An intermediate case, where the sample was quickly cooled by turning the substrate heater off after 5 min, was also tried. The Al_2O_3 films grown and studied for this thesis ranged in thickness from 15 to 125 Å.

The growth temperature of 800 °C was chosen by comparing RHEED patterns from growths over a range of temperatures. Figure 5.1 shows two RHEED images, one from a growth done at 700 °C, the other done at 830 °C. The lower-temperature growth has broader streaks and shows more diffuse electron scattering, while the

higher-temperature growth shows sharper streaks in a darker background. To illustrate this more clearly, I also show in Figure 5.1 a line-scan of each image. The difference in streak widths and background intensity is clearly seen in the plot.

Sharper RHEED streaks are desirable because they indicate a qualitatively better crystal structure. This is because the streak width is directly proportional to the width of the reciprocal space rod. The alumina films shown in Figure 5.1 have normalized streak widths, $(\Delta q)/q$, of 0.18 and 0.24 for growth at 830 °C and 700 °C, respectively. For this reason, growths of epitaxial alumina on annealed niobium were carried out near 800 °C. These data suggest that higher temperature is better. However, growths were not carried out higher than 830 °C, in the hope of avoiding niobium oxidation or Nb-Al mixing at the interface.

5.1.2 Materials Analysis

Chemical analysis of Al_2O_3 films was carried out in the adjacent XPS system. The challenge with doing XPS on an insulator such as alumina is that it tends to charge. The effect this has is to shift the binding energies toward higher values – photoelectrons have a slightly reduced kinetic energy due to the positively charged surface of the sample. Charging can also broaden the peaks associated with elements of the insulating layer, as the photoelectrons originate a different depths and therefore cross different potentials upon exiting the sample. Despite these shortcomings, measurements of the Al^{3+} $2p$, O^{2+} $1s$ and Nb $3d$ levels suggest that the Al is completely oxidized with no measurable oxidation of the underlying Nb. In Figure 5.2 I show the scans from a 20 Å Al_2O_3 grown on annealed Nb (110). Both the Al^{3+} $2p$ and O^{2+} $1s$ peaks can be fit with a single curve, while two curves suffice to fit the Nb $3d$ peaks. The observed energy difference between the O^{2+} $1s$ and Al^{3+} $2p$ levels is 457.1 eV, in good agreement with what has been reported for sapphire (456.6 eV) [58]. The Nb $3d$ level shows no side-bands that would indicate oxide

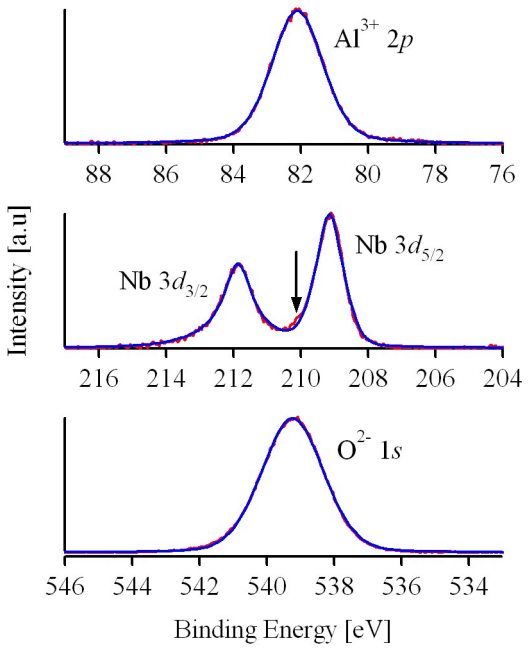

Figure 5.2: XPS scans from an epitaxial Al_2O_3 thin film on niobium. All peaks are fit as described in the text, with the aluminum completely oxidized and the niobium fully metallic. The small shoulder on the Nb $3d_{5/2}$ peak may indicate partial oxidation at the interface with the alumina over-layer.

formation. However, I point out that the Nb $3d_{5/2}$ peak shows a small hump that may indicate interfacial oxidation. This issue was not extensively investigated.

RHEED of the Al_2O_3 thin films on annealed Nb (110) revealed a hexagonal symmetry in the surface lattice, indicating basal-plane growth. However, no ordering of the Al sublattice was ever observed in the RHEED patterns. Because all of the alumina polymorphs involve the stacking of close-packed oxygen planes, no definitive crystal structure could be inferred. By convention only though, I will use hexagonal Miller indices corresponding to the α-Al_2O_3 lattice to describe crystal orientations in my films.

Diffraction images from various stages of deposition are shown in Figure 5.3. Immediately after the oxide deposition begins, the Nb diffraction pattern and specular spot disappear. After about 2 ML (4 Å) the Al_2O_3 diffraction pattern becomes

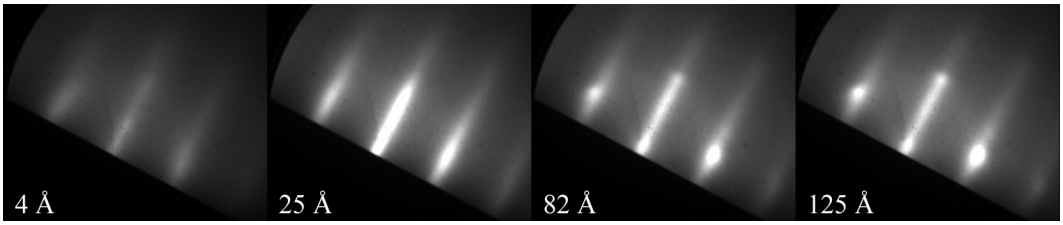

Figure 5.3: RHEED from various stages of Al_2O_3 hetero-epitaxy on annealed Nb (110). Initially the film shows a 2D RHEED pattern, but beyond about 50 Å the diffraction image evolves to one that shows transmission spots. This indicates a shift from layer-by-layer growth to island growth.

visible. At a thickness of 25 Å, RHEED shows an elongated specular spot and well-defined first-order streaks. Up to about 50 Å, the Al_2O_3 growth is layer-by-layer (Frank-van der Merwe mode). Beyond this thickness, the 2D streaks evolve into 3D spots, indicating the growth of islands (Stranski-Krastanov mode).

Ex situ AFM confirmed this evolution of the alumina surface morphology, as shown in Figure 5.4. Scans of a 20 Å-thick film showed an atomically flat surface with large terraces several 100 nm in width, and monolayer step-edges ($c/6 = 2.165$ Å) aligned according to the substrate miscut. Overall, the films shows an rms roughness of about 2 Å. On the other hand, the surface of a 100 Å-thick film consisted of islands. These islands were, on average, about 1000 Å wide and 50 Å in height. This morphology agreed well with the interpretation of Al_2O_3 RHEED – evidence for islands in the diffraction images appeared after about 50 Å of deposition.

In addition to the evolving nature of the alumina surface, RHEED also shows that the epitaxial Al_2O_3 film is slightly misaligned with the Nb surface. Using the RHEED pattern from the niobium surface and, specifically, the Kikuchi lines, the sample was precisely aligned with the RHEED beam along the Nb $[\bar{1}11]$ azimuth. With the sample oriented in such a way, the RHEED from the alumina over-layer was slightly misaligned. This was evidenced by the asymmetry in the RHEED pattern, as shown in Figure 5.5. Compared with the right-hand 1^{st}-order streak, the left-hand streak showed an intensity that was, on average, about 35% smaller. That the

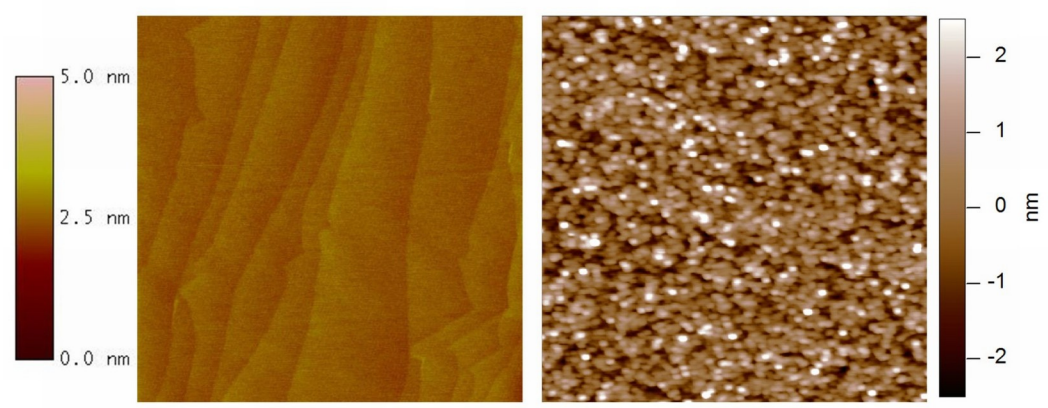

Figure 5.4: A comparison of AFM scans on Al_2O_3 thin films on annealed Nb (110). Left: A 20 Å-thick film, showing large terraces and monolayer step-edges. Right: A 100 Å-thick film comprised of islands that are, on average, about 1000 Å wide and 50 Å in height. Both images are 5×5 μm^2, and respective height scales are shown.

alumina RHEED appears slightly misaligned indicates a possible NW orientational relationship between the niobium surface and the oxide over-layer. With RHEED evidence alone, however, this finding is far from definitive.

The third piece of information that can be extracted from RHEED is the strain of the surface lattice. As was mentioned in Chapter 4, the niobium RHEED can be used as a ruler, due to its unstrained nature. Using images from more than 20 samples I found a System E RHEED coefficient, β of 616 ± 4 Å-pixels. β was determined using Nb RHEED from just before Al_2O_3 deposition (at 800 °C) and the bulk niobium lattice constant (a = 3.3066 Å at 25 °C). Because of thermal expansion, this value of β is probably too small by about 0.5% – both Nb and Al_2O_3 have expansion coefficients around 7–8$\times 10^{-6}$ K^{-1} [59, 60, 61]. For the strain measurements reported here, however, I used $\beta = 616 \pm 4$ Å-pixels. The variation in β is largely due to the ability to move the RHEED beam around on the sample. The sample-to-RHEED screen distance is about 32 cm, so moving the electron beam $\pm$ 3 mm constitutes a 1% error in any measure of k-spacing. During the growth of an Al_2O_3 film, however, the beam and sample were left fixed and the film strain as

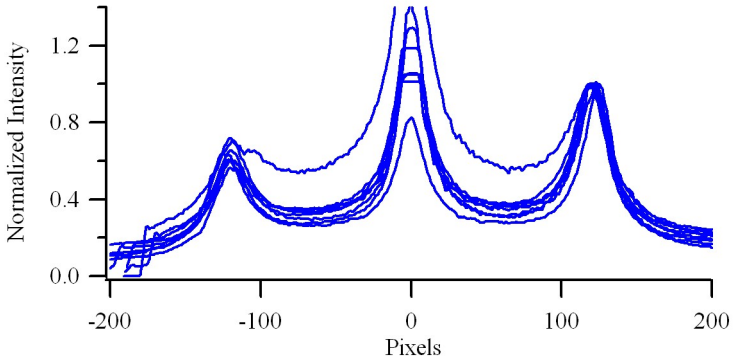

Figure 5.5: This plot shows the misalignment of the Al_2O_3 over-layer with the Nb film. The sample is rotated such that the RHEED beam is along the Nb [$\bar{1}$11] azimuth, and these are a series of line scans showing the intensity of RHEED streaks, each scan showing results from a different growth. The intensity profiles are normalized to the right-hand 1st-order streak. The left-hand 1st-order streak is on average 36% less intense.

a function of film thickness could be measured with a higher precision.

As the transformation from 2D to 3D alumina growth was occurring, the measured spacing between RHEED streaks/spots increased, indicating a shrinking of the Al_2O_3 surface lattice. The Al_2O_3 film experiences a tensile strain due to lattice misfit that relaxes with increasing thickness, as shown in Figure 5.6. The strain-thickness curve was determined from RHEED along the [$\bar{1}$100] azimuth during Al_2O_3 deposition near 800 °C. With respect to C-plane sapphire ($a = 4.759$ Å), the tensile strain was nearly 10% initially and by 20 Å had fallen to about 8%. After 100 Å of deposition, the Al_2O_3 exhibited a tensile strain of around 3%.

After deposition and cooling in O_2, Al_2O_3 films of various thicknesses show further lattice relaxation (Figure 5.6). On average, RHEED measurements near room temperature show a strain reduction of about 1% when compared to measurements just after Al deposition. Thermal contraction accounts for a significant portion of the strain change during cooling. Due to the limited precision of the measurement technique, the presence of other strain-relief mechanisms could not be determined. As Goodman points out [30], misfits as large as the ones found in the Nb/Al_2O_3

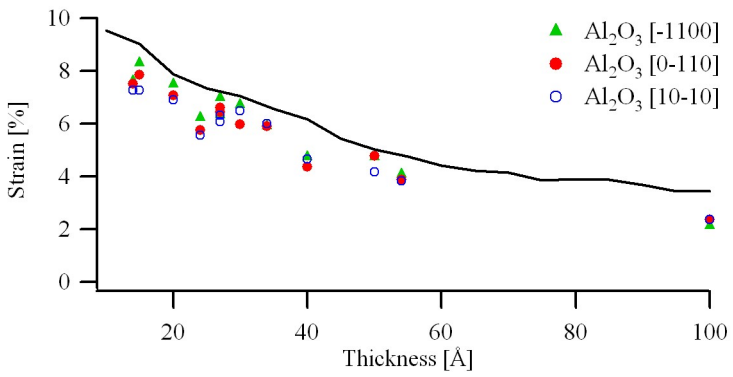

Figure 5.6: Strain vs. thickness for epitaxial Al_2O_3 thin films deposited on annealed Nb (110). The line shows the strain relaxation during deposition for a single growth at 800 °C, while the various data points show the strain measured along different Al_2O_3 azimuths near room temperature.

system are likely to generate dislocations and domain wall structures. However, neither of these features were ever observed in 20 Å alumina films.

Not only is there a large strain in the Al_2O_3 film, but the strain is also isotropic – RHEED patterns along the $\{\bar{1}100\}$ azimuths reveal relatively small variations. The strain for each azimuth is determined by averaging opposite directions – eg. $[\bar{1}100]$ and $[1\bar{1}00]$ – to reduce systematic errors. The measured tensile strain for the three principal Al_2O_3 azimuths is shown in Figure 5.6. One might expect an anisotropic strain due to the asymmetric misfit of the Al_2O_3 (0001) lattice with the Nb (110) lattice. However, the surface of the niobium is tiled with NbO (111) due to the reconstruction. Epitaxial aluminum oxide on annealed Nb (110) grows under isotropic tensile strain because of this NbO (111) surface net.

I show in Figure 5.7 the surface lattices for bulk Nb (110) and NbO (111), as well as that for C-plane sapphire, α-Al_2O_3 (0001). For both of the oxides, only the cation sublattice is shown, for the sake of clarity. If the aluminum oxide film initially grows clamped to the niobium surface then the measured strain would simply equal the lattice misfit. The misfit between Nb (110) and Al_2O_3 is very asymmetric: along the Nb [001] or α-Al_2O_3 $[\bar{1}100]$ direction it is quite large (20.3%), while along the

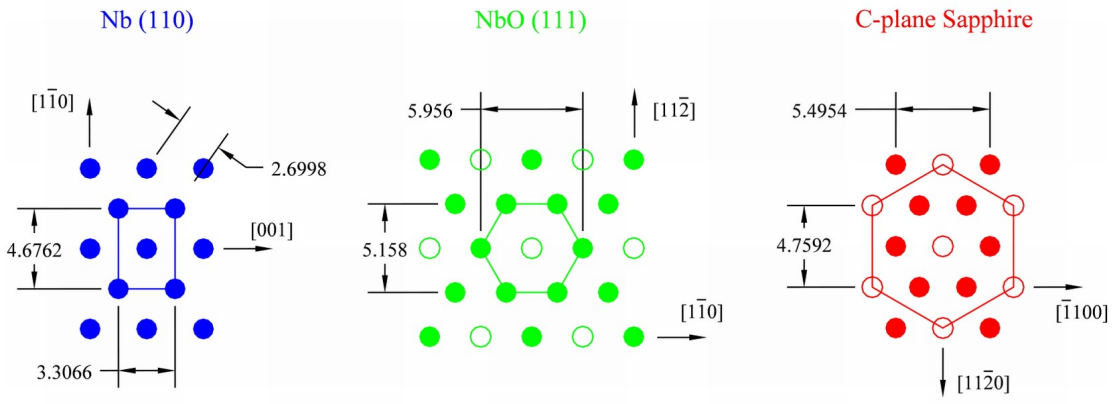

Figure 5.7: Comparison of surface lattices for Nb (110), NbO (111) and C-plane sapphire, α-Al_2O_3 (0001). For the oxides only the cation sublattices are shown, and all dimensions are given in units of angstroms.

Nb [$\bar{1}$10] or α-Al_2O_3 [11$\bar{2}$0] it is much smaller, with the alumina lattice slightly bigger (-1.7%). However, the niobium lattice has no influence on the hetero-epitaxy of Al_2O_3.

Instead, aluminum oxide on annealed niobium grows pseudomorphically on the NbO (111) surface layer. The fcc-based structure yields a hexagonal surface net in the (111) orientation, providing for an isotropic misfit of 8.4%. This number agrees quite well with the strain values measured for ultra-thin alumina films on annealed niobium; 15 Å films showed about 7.5–8.0% strain. In the absence of this NbO (111) surface net though – for Al_2O_3 films on unannealed Nb (110) – I find the strain to be very asymmetric.

5.2 Al_2O_3 Hetero-Epitaxy on Unannealed Nb (110)

5.2.1 Growth Procedures

The growth procedure for Al_2O_3 on unannealed niobium films was slightly different than that for growth on annealed niobium, primarily out of a concern for oxidizing the underlying metal. Annealed niobium, with its surface reconstruction, would seem likely to resist further oxidation better than unannealed niobium. For that reason, alumina was deposited on unannealed Nb (110) at a slightly lower substrate temperature, around 750 °C. In addition to the lower temperature, the deposition was also initiated with a lower oxygen background pressure of 5×10^{-8} torr. Once the substrate mask had been pulled back and the growth had begun, the O_2 pressure was then raised to 5×10^{-6} torr. Al_2O_3 films grown on unannealed Nb (110) ranged in thickness from 20–36 Å.

5.2.2 Materials Analysis

As with Al_2O_3 hetero-epitaxy on annealed Nb (110), RHEED was employed to determine the alignment of the alumina over-layer on unannealed niobium. In a similar fashion, the sample was aligned with aid of the Kikuchi lines such that the RHEED was oriented along the Nb $[\bar{1}11]$ azimuth. In contrast with the results from growth on annealed niobium, the Al_2O_3 film grows aligned with the Nb $[\bar{1}11]$ direction. A set of line scans, similar to those in Figure 5.5, are shown for alumina hetero-epitaxy on unannealed Nb (110) in Figure 5.8. Again, the intensities of the scans are normalized to the right-hand 1^{st}-order streak. The left-hand streak shows a minimal decrease in intensity – on average it is only about 3% smaller. The alignment of the alumina film with the Nb (110) lattice is suggestive of the KS

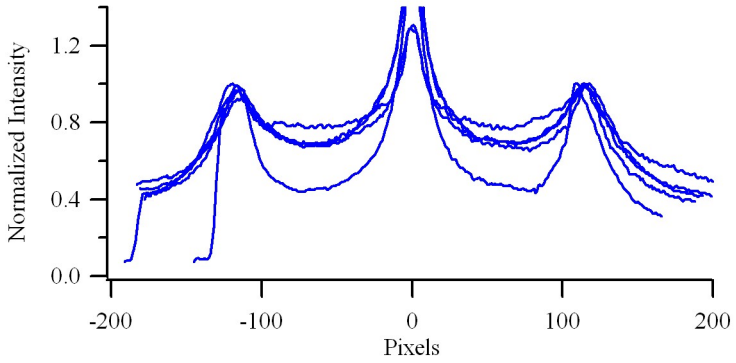

Figure 5.8: This plot shows the alignment of the Al_2O_3 over-layer with the Nb film. The sample is rotated such that RHEED is along the Nb [$\bar{1}$11] azimuth, and these are a series of line scans showing the intensity of RHEED streaks, each scan showing results from a different growth. The intensity profiles are normalized to the right-hand 1st-order streak. The left-hand 1st-order streak shows a nearly equivalent intensity.

orientational relationship – similar to that found on Ta [10] – though no absolute determination can be made on this evidence alone.

As suggested in the previous section, strain measurements for aluminum oxide hetero-epitaxy on unannealed Nb were also quite different from those on annealed Nb. In this case the strain is very asymmetric, as shown in Figure 5.9, indicating a pseudo-hexagonal surface lattice. In Figure 5.9 I denote the Al_2O_3 azimuths by their nearest-to-parallel Nb directions. RHEED along what was originally the Nb [001] direction shows a strain that starts small (1.5% at 20 Å), increases to a maximum of about 5% at 26 Å and then slowly relaxes. On the other hand, strain levels along the Nb {$\bar{1}$11} azimuths starts high (9% at 20 Å) and decreases monotonically. As the thickness of the Al_2O_3 film increases, the strain anisotropy also decreases.

As was mentioned in the previous section, Al_2O_3 hetero-epitaxy on unannealed niobium should be subject to a 20.3% misfit along the Nb [001] or α-Al_2O_3 [$\bar{1}$100] directions and a -1.7% misfit along the Nb [$\bar{1}$10] or α-Al_2O_3 [11$\bar{2}$0] directions. The latter misfit is accessible by doing RHEED measurements along the Nb [001] azimuth. RHEED along the Nb [$\bar{1}$11] corresponds with the (211) planar spacing, which

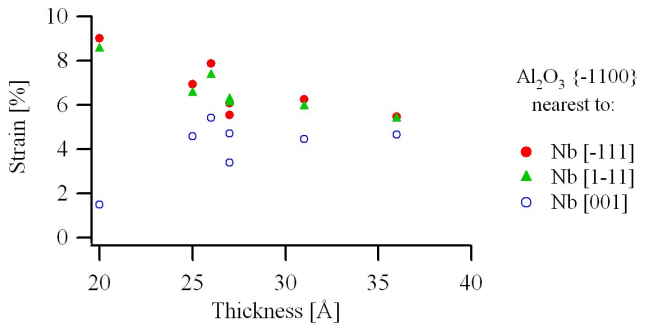

Figure 5.9: Strain vs. thickness for epitaxial Al_2O_3 thin films deposited on unannealed Nb (110). The different RHEED azimuths are distinguished by the nearest Nb direction. The measured strain for all thicknesses is asymmetric due to the anisotropic misfit with the underlying niobium.

is about 13.4% larger than the planar spacing in C-plane sapphire. Extrapolating from a minimum film thickness of 20 Å my measurements agree qualitatively with the theoretical misfits. So while Al_2O_3 films on annealed niobium show a hexagonal surface lattice, those on unannealed niobium have what can best be described as a pseudo-hexagonal lattice that arises in order to accommodate the asymmetric misfit with the under-layer.

5.3 Epitaxial Niobium Over-Layers

A majority of Nb/Al_2O_3 bi-layers were coated with a niobium over-layer for the purpose of making tunnel-junctions. For that deposition, the sample was transferred back to System F. Most samples were finished with a top niobium layer grown at room temperature – done in an effort to reduce possibility of reactions at the alumina/Nb interface. In a few cases however, that Nb over-layer was epitaxial, for which the substrate was warmed back up to about 700 °C. Otherwise, the growth conditions for the top niobium layer were identical to those for the base layer.

Under these conditions (growth at 700 °) niobium growth on C-plane sapphire would yield (111)-oriented films according to the three-dimensional relationship

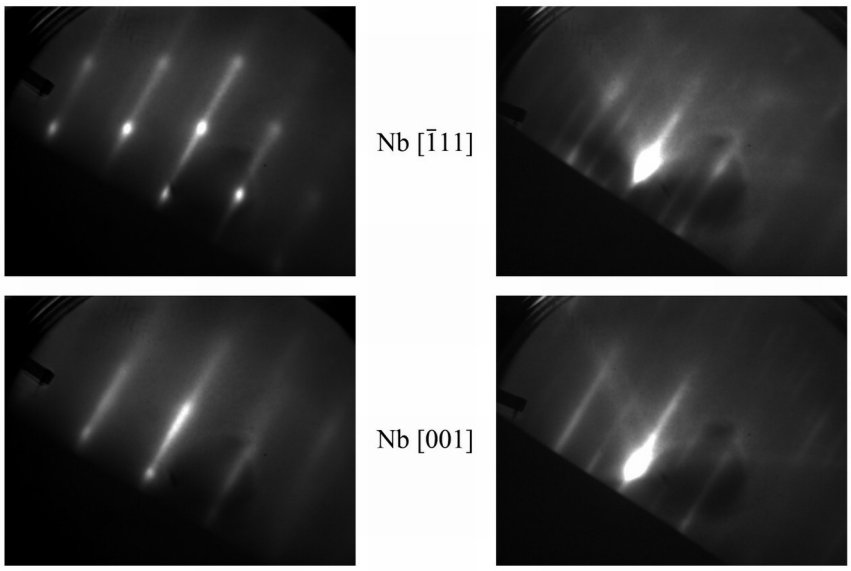

Figure 5.10: RHEED images from epitaxial niobium films on single-crystal Nb/-Al_2O_3 bi-layers. Both films were deposited at around 700 °C on $\sim$ 25 Å-thick alumina films grown on annealed (left) and unannealed (right) Nb (110) surfaces. While samples with unannealed base layers showed familiar Nb (110) RHEED, those with annealed base layers showed transmission patterns, indicative of island growth.

(Fig. 4.1) [6, 40]. However, for samples with both annealed and unannealed base layers, the RHEED patterns looked decidedly like (110) surface diffraction. A comparison of the RHEED in each case is shown in Figure 5.10 – for each sample the alumina layer was about 25 Å thick. For those samples with *unannealed* base-layer niobium (and pseudo-hexagonal aluminum oxide) the top niobium film appears to have grown as if the alumina layer was not there. Sharp 1st-order streaks, Kikuchi lines, intermediate streaks indicative of the as-grown surface reconstruction – all the same features were present in these patterns that were there for the base layer (see Fig. 4.2). On the other hand, samples with *annealed* base-layer niobium and hexagonal alumina showed top-niobium epitaxy that grew in islands. This much was clear from the transmission images. The patterns were still indicative of Nb (110) growth, just not layer-by-layer epitaxy.

Ex situ XRD analysis confirms the surface orientation of the top layer niobium

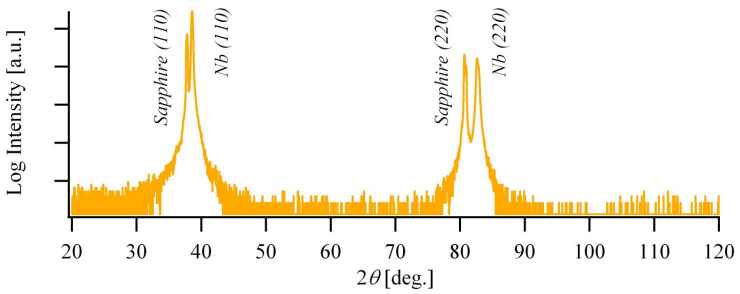

Figure 5.11: Radial XRD scan of an all-epitaxial $Nb/Al_2O_3/Nb$ tri-layer. Both the base and top niobium layers grow single-crystal in the (110) orientation.

– same (110) orientation as the base layer. Radial scans (see Figure 5.11) show only the Nb (110) and (220) reflections. The Nb (222) Bragg peak, if present, would appear in the scan at $2\theta = 108°$.

A number of epitaxial tri-layers were also examined by doing a ϕ-scan to determine in-plane orientations. Three representative ϕ-scans are shown in Figure 5.12. For the case where the base niobium film is *unannealed* and the alumina intermediate layer is pseudo-hexagonal, the top niobium film grows with only one in-plane orientation, in alignment with the base niobium. Again, the crystal lattice of the base layer appears to have been carried through the thin alumina film. The four Bragg peaks do have two components each though: a narrow one attributed to the bottom niobium layer and a broad one for the top. The widths of these components are $\Delta\phi_b \approx 0.4°$ and $\Delta\phi_t \approx 1.6°$ for the bottom and top layers, respectively. This indicates a poorer crystallinity in the niobium over-layer likely due both the intermediate Al_2O_3 layer and the lower growth temperature.

With an *annealed* niobium base layer and a hexagonal alumina film, the top niobium layer shows three domains rotated 120° with respect to each other. The dominant domain is slightly misaligned with the base layer (about 2.2°) and comprises nearly 90% of the top niobium layer. The origin of the 2.2° is unknown, especially considering that the two orientational relationships (NW and KS) involve

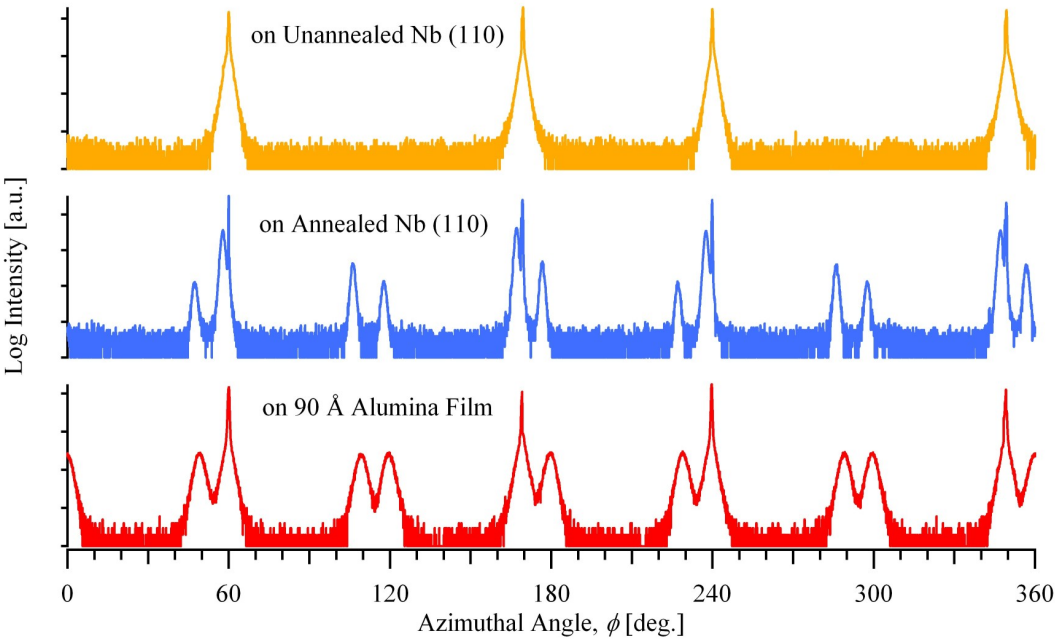

Figure 5.12: ϕ-scans of off-specular Nb {110} Bragg peaks for epitaxial Nb/Al_2O_3/-Nb tri-layers. The plots demonstrate the difference between unannealed (top) and annealed (middle) base niobium layers – in each of these cases the Al_2O_3 film was about 25 Å thick. For comparison, the bottom scan is from an epitaxial tri-layer with 90 Å-thick Al_2O_3.

an angle of 5.26° between substrate and over-layer. Intensity peaks corresponding to the bottom niobium layer ($\Delta\phi_b \approx 0.3°$) again show better crystallinity than those for the top ($\Delta\phi_t \approx 1.4°$).

The existence of a dominant domain is also intriguing, and points toward an asymmetric or otherwise irregular cation lattice in the Al_2O_3 film. RHEED tells us only that the oxygen anion lattice is hexagonal, at least to the level of precision of our RHEED system. And recalling the building principle of Gutekunst *et al.* [41] – that niobium on sapphire grows in a manner dictated by the Al sublattice – the preferential growth of the niobium top layer with an in-plane direction slightly misaligned with the base layer is suggestive of an asymmetric cation sublattice. An asymmetric cation lattice in the Al_2O_3 film may be caused by the tensile strain, or simply due to it taking the form of an alumina polymorph. It may also be the

case that the Al sublattice is disordered, in which case the building principles are probably irrelevant.

The third ϕ-scan shown in Figure 5.12 is for a sample where the base niobium layer was unannealed and the Al_2O_3 film thickness was 90 Å, considerably thicker than the other samples. In fact, by 90 Å the alumina layer would have started to grow in island-mode and one would expect the surface lattice to be hexagonal, regardless of the thermal treatment of the underlayer. (Even by 36 Å Al_2O_3 films on unannealed niobium were showing nearly isotropic strain – see Fig. 5.9) On alumina this thick though, the top niobium layer grew with three equally populated domains, one of which was perfectly aligned with the base niobium film.

If one assumes that niobium hetero-epitaxy on thin (and strained) Al_2O_3 films proceeds as has been observed for growth on C-plane sapphire – that is with Nb [001] $\parallel$ α-Al_2O_3 [$\bar{1}$100], [0$\bar{1}$10] and [10$\bar{1}$0] – then tri-layers with thick alumina have the Al_2O_3 film NW-oriented. While this seems like a reasonable assumption, for the other cases – those tri-layers with $\sim$ 25 Å alumina – the evidence points toward more unique behavior.

Finally, I present here some TEM work done by the Zuo group on one of my Nb/Al_2O_3/Nb tri-layers. The image shown in Figure 5.13 is taken from a sample with an unannealed base niobium layer, a 20 Å-thick oxide film, and a poly-crystalline niobium over-layer deposited at room temperature. The interface between the oxide and the base layer is atomically sharp and defect free. However, the niobium *over-layer* appears to have dissolved regions of the alumina film. 20 Å of basal-plane Al_2O_3 corresponds to about 9 mono-layers, and in this image a maximum of 6 can be seen, and in some regions only 2 are visible. This mixing at the interface between the alumina and niobium over-layer was completely unexpected, especially considering that the top niobium was deposited at room temperature. To the best of my knowledge this has never been observed in niobium films on sap-

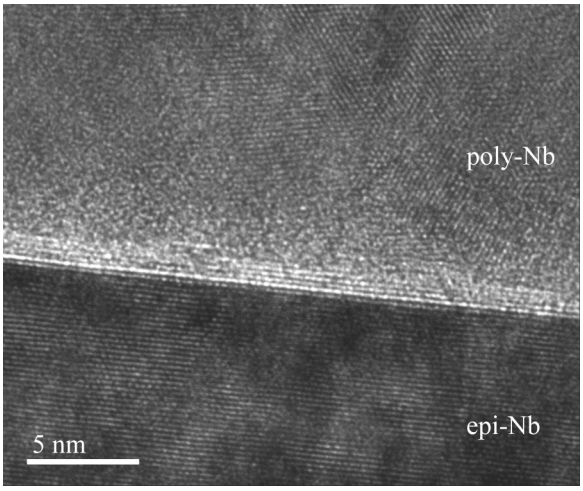

Figure 5.13: A TEM image for a $Nb/Al_2O_3/Nb$ tri-layer. This particular sample had an unannealed base layer and a poly-crystalline top layer grown at room temperature. While the alumina interface with the base layer appears defect-free, regions of the oxide layer appear to have been dissolved by the niobium over-layer.

phire, so in the tri-layers mixing may be due to some property of the alumina film. Regardless of the cause, the dissolving of the barrier had a devastating effect on tunnel-junctions fabricated from these tri-layers.

5.4 Epitaxial Alumina as a Barrier in Tunnel-Junctions

Josephson tunnel-junction devices fabricated from epitaxial bi-layers and tri-layers were consistently very poor in quality – so poor that it might not even be accurate to refer to them as such. I show in Figure 5.14 a number of I-V characteristics that are typical of the entire data set. Devices with oxide layers 20 Å thick usually had critical currents greater 20 mA, and currents of 100 mA were often incapable of reaching the niobium gap voltage ($\sim$ 3 mV). Even when the gap voltage was reached, there was no signature in the I-V curve.

Devices with annealed niobium base layers showed a moderate thickness depen-

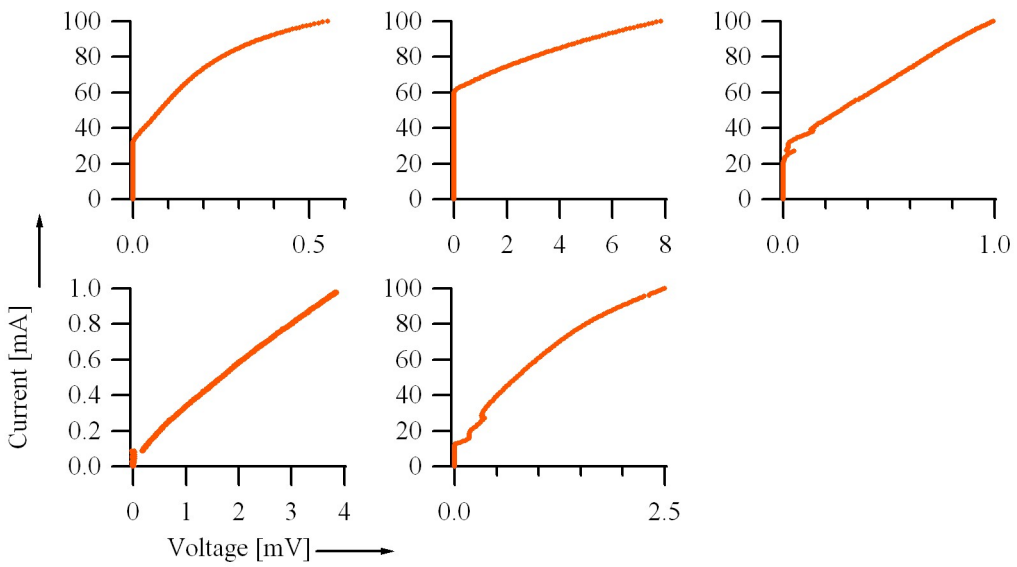

Figure 5.14: Current-voltage characteristics for a number of tunnel-junctions fabricated from epitaxial Nb/Al_2O_3. Included here are devices with both annealed and unannealed base-layer Nb, both epitaxial and poly-crystalline top-layer Nb, and oxide thicknesses ranging from 20–54 Å.

dence, with I_c dropping by a decade about every 15 Å. Those with unannealed niobium showed a much weaker dependence with only half a decade dropped over roughly 30 Å. Despite the overall poor device quality this is an interesting contrast to consider. At this point, it is unclear whether this difference is due to the presence of the NbO surface layer, or caused by differences in strain.

However, it does seem reasonable to attribute the poor device performance to the mixing observed at the interface between the oxide barrier and over-layer niobium. Such mixing could create electrical "pinholes" – nanometer-size regions with a significantly lower tunneling barrier height than the rest of the junction. In communications with Seongshik Oh I have learned that, despite the success with Re/Al_2O_3/Al tri-layers [13], tunnel-junctions fabricated from Re/Al_2O_3/Re tri-layers were very "leaky" – perhaps rhenium was mixing with the oxide layer just as I've observed with niobium.

5.5 Summary

In summary, single-crystal Nb/Al_2O_3 and $Nb/Al_2O_3/Nb$ multi-layers were grown by MBE. Various methods of materials analysis suggest these layers were all high-quality. The alumina films showed good stoichiometry with no oxidation of the niobium base layer. And a transition in the Al_2O_3 epitaxy from layer-by-layer growth to island growth was observed to occur at a film thickness of about 50 Å.

The principal finding though is that epitaxial growth of Al_2O_3 on Nb (110) is highly dependent on the niobium surface reconstruction. Alumina films on *annealed* Nb grow misaligned with the Nb $[\bar{1}11]$ direction, are isotropically strained, show a hexagonal surface lattice, and give rise to multi-domain epitaxial Nb over-layers. In contrast, those on *unannealed* Nb grow aligned with the $[\bar{1}11]$ direction, show an asymmetric strain and a pseudo-hexagonal lattice, and yield single-crystal Nb over-layers that mimic the base layer. Epitaxial niobium over-layers on thick alumina showed a still different behavior that was suggestive of a NW type orientational relationship.

Another important finding came from TEM work done on a $Nb/Al_2O_3/Nb$ tri-layer. Images revealed an atomically sharp interface between the oxide and base layer, but mixing was seen to occur with the deposition of the over-layer. This mixing undoubtedly had a substantial effect on tunnel-junctions fabricated from these tri-layers. While devices did show very poor qualities, the employment of an aluminum counter-electrode may go a long way toward solving this issue. And by eliminating any barrier deterioration by the over-layer, one may ultimately be able to study the effects of alumina strain in Josephson junction devices.

Chapter 6

Tunnel Junctions from Epitaxial Nb/Al Bi-Layers

In 3.2.1 I reviewed previous attempts to fabricate Josephson tunnel-junctions from epitaxial Nb/Al bi-layers. Only in the case of sputtered films was success found [34]. Here I report on my own work involving the fabrication of tunnel-junctions from epitaxial Nb/Al bi-layers grown by MBE. I discuss both the materials properties and device characteristics.

6.1 Al Hetero-Epitaxy on Nb (110)

Aluminum, with its fcc crystal structure, can be expected to grow in the (111) direction on Nb (110). The ratio of lattice parameters – $a_{\mathrm{fcc}}/a_{\mathrm{bcc}} = 1.227$ – places this pair between calculated energy minima for the KS and NW orientational relationships [26, 27, 28, 29]. Experimentally, only the NW orientation has been reported [62, 63]. In this section I describe my own work on Al hetero-epitaxy on Nb (110) films.

6.1.1 Growth Procedures

Epitaxial aluminum metal over-layers were deposited at room temperature on unannealed Nb (110) films. Evaporation rates for Al varied from 1-3 Å/s, which required a cell temperature of up to 1200 °C. The chamber pressure during deposition was typically around 1×10^{-9} torr. The thickness of the aluminum films grown for this work varied from 60–520 Å.

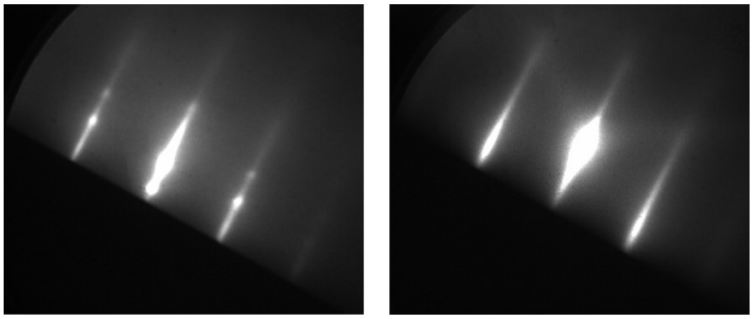

Figure 6.1: RHEED images from Al (111) films grown on unannealed Nb (110). The films shown here are 65 Å (left) and 470 Å (right) thick.

The formation of an aluminum oxide layer – for the purposes of making tunnel-barriers – was achieved in one of two ways. The first involved simply exposing the aluminum film to O_2 in the load-lock, similar to the Gurvitch process [5]. Oxygen gas was fed to the load-lock from the same UHP O_2 manifold used to inject gas into the growth chamber. The sample was allowed to sit for one hour in an O_2 atmosphere of either 10 or 100 torr. The thickness of the oxide in this case is limited by a combination of exposure and diffusion.

The second process involved the co-deposition of Al and O_2 in the MBE chamber. After the growth of an aluminum layer – sufficiently thick for complete niobium coverage – an AlO_x film was formed by evaporating Al at a rate of about 0.1 Å/s at room temperature in an O_2 background of 5×10^{-6} torr. The stoichiometry of the as-grown oxide was limited by thermodynamics. To improve the stoichiometry – I suspected an oxygen-deficient film – the sample was exposed to O_2 in the load-lock, as described above. To complete the tri-layer, a niobium top layer was deposited at room temperature under otherwise similar conditions to the base-layer niobium growth.

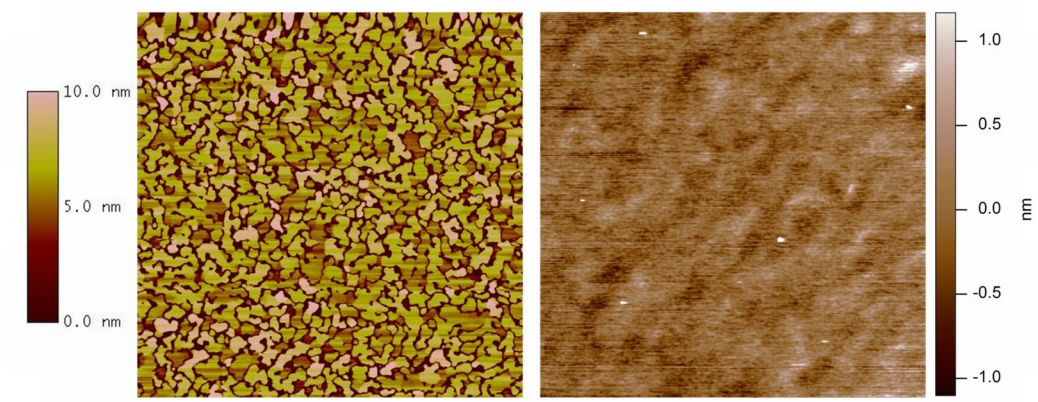

Figure 6.2: AFM scans of Al (111) films that were 65 Å (left) and 200 Å (right) thick. The trenches seen in the thin film go all the way through to the underlying niobium. Thicker continuous films were required for making tunnel-junctions.

6.1.2 Materials Analysis

In situ RHEED shows the progression of the Al surface during deposition. In Figure 6.1 I show RHEED patterns for films at both ends of the explored thickness range. Thinner films ($\lesssim$ 100 Å) showed superimposed RHEED and transmission patterns, indicating a mixed morphology of flat regions and islands. Beyond about 100 Å the transmission spots would disappear and the diffraction images would show nice RHEED streaks indicative of a flat surface.

Ex situ AFM measurements confirmed this morphology distinction between films of different thicknesses. As shown in Figure 6.2, a 65 Å film had meandering trenches that penetrated through the entire aluminum thickness. Aside from these trenches and a scattering of asperities, the surface over large areas was fairly flat. (Because of the similar growth conditions and film thickness, I suspect that it was this lack of niobium coverage that caused the devices of Braginski *et al.* to be of such poor quality [33].) On the other hand, a 200 Å film showed no such trenches or pinholes. It was this flat aluminum surface that was required for making tunnel-junctions.

Finally, XRD analysis was performed on Nb/Al bi-layers – a radial scan of one such sample is shown in Figure 6.3. Despite their proximity to one another, both

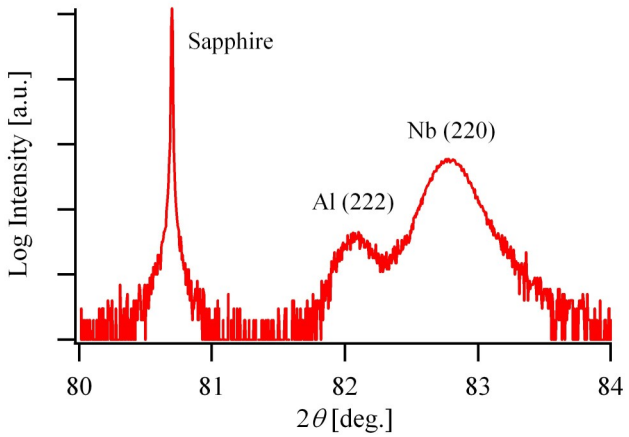

Figure 6.3: Radial XRD scan of an epitaxial Nb/Al bi-layer grown on A-plane sapphire. For this sample the Nb layer was 1000 Å thick and the Al layer 500 Å thick.

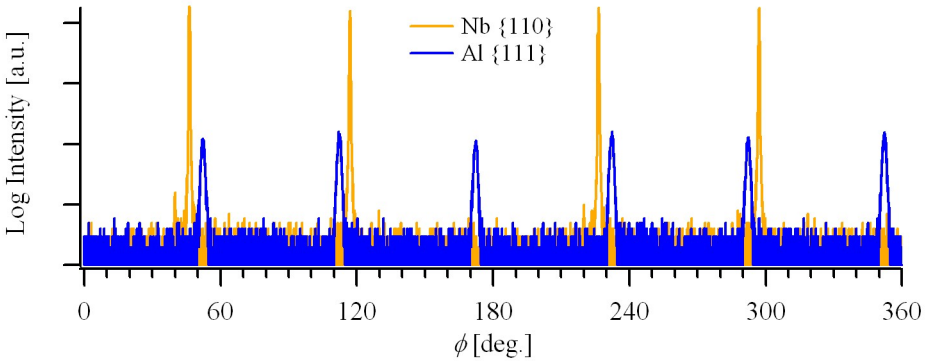

Figure 6.4: ϕ-scans for a Nb/Al bi-layer showing the non-specular Nb {110} and Al {111} Bragg peaks. The scans indicate both a NW orientational relationship and twinning in the Al film.

the Nb (220) and Al (222) Bragg peaks could be resolved using the high-resolution diffractometer. No other specular Bragg peaks were observed, confirming that the Al film was indeed single-crystal. This scan is very similar to the one observed by Kirk *et al.* [34] for Nb/Al bi-layers grown by sputtering.

ϕ-scans are shown in Figure 6.4 – included are the non-specular Nb {110} and Al {111} Bragg peaks. These scans confirm the NW-type orientational relationship between the fcc Al and bcc Nb. They also indicate twinning in the aluminum film which arises due to the two fcc (111) stacking variants: $ABC\ldots$ and $ACB\ldots$

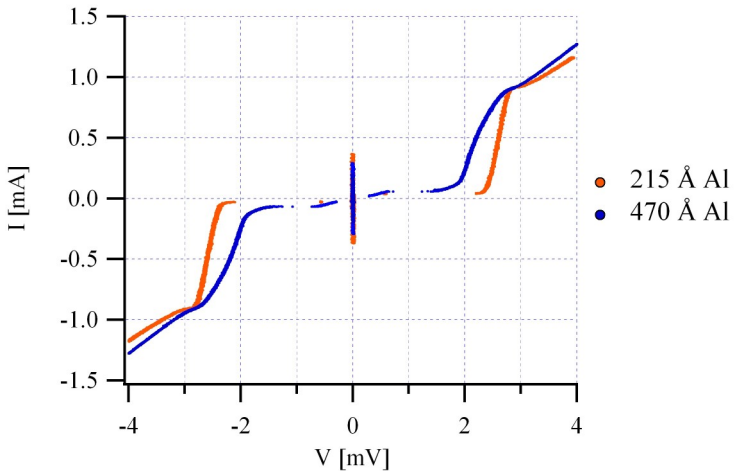

Figure 6.5: Current-voltage characteristics for two devices, one with 215 Å Al (left) and one with 470 Å Al. Devices shown here are 10×10 μm^2.

6.2 Josephson Junctions with Oxidized Epitaxial Al Barriers

My study of Josephson tunnel-junctions fabricated from epitaxial Nb/Al bi-layers was a fairly brief one. The devices I describe here served not only a scientific purpose but a practical one as well – they verified the reliability of both the fabrication process and the testing setup. In scientific terms, my results have significance because they represent the first case of tunnel-junctions fabricated using a Gurvitch-style process [5] from epitaxial Nb/Al bi-layers grown by MBE. Additionally, the current-voltage (I–V) characteristics of the junctions show remarkable agreement with theory, despite the fact that thicker Al layers ($\geq$ 200 Å) were used. Included in this data set are samples with variable Al thickness, O_2 exposure, and co-deposited AlO_x thickness.

Because superconductivity in the aluminum layer is induced by the proximity effect, devices with different Al thicknesses show contrasting behavior. In Figure 6.5 I show the I–V characteristics of two devices measured at 4.2 K, one with 215 Å of Al and the other with 470 Å. For both samples, the aluminum layer was exposed to

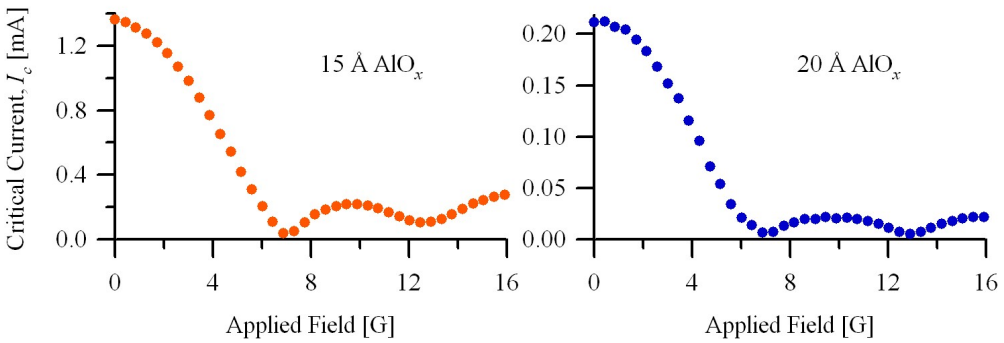

Figure 6.6: Fraunhofer patterns for devices with 15 Å (left) and 20 Å (right) of co-deposited AlO_x. These devices measure 30×30 μm^2.

10 torr of O_2 for one hour (3.6×10^7 L). The device with 215 Å Al shows a lower sub-gap resistance at 1.5 mV ($\sim 38\ \Omega$) than the device with 470 Å ($\sim 24\ \Omega$). The thinner Al also gives rise to a narrower gap-width, 0.5 eV, compared with 1.0 eV for the thicker Al layer. Outside of the sub-gap structure there is little that distinguishes the two devices. The critical currents, I_c, and normal-state resistances, R_n, are comparable – 0.37 mA and 3.4 Ω (215 Å Al) versus 0.29 mA and 2.9 Ω (470 Å Al). Devices where the Al was given 10 times the O_2 exposure showed no significant differences with these devices.

Aside from two samples with thicker aluminum, all the devices had Al layers about 200 Å thick. Among these there were three different barriers studied: (1) oxidation of Al metal done only in the load-lock; (2) 15 Å of co-deposited AlO_x plus load-lock oxidation; and (3) 20 Å of co-deposited AlO_x plus load-lock oxidation. In each case, the measured I_c was about 50% of the theoretical maximum, $I(2\Delta)\pi/4$. However, the critical current density, J_c, varied from 350 A/cm^2 for process (1), to 160 and 25 A/cm^2 for processes (2) and (3), respectively.

I examined the dependence of some of these junctions on applied magnetic field. In all cases the field was applied parallel to the junction (in the plane of the barrier) and perpendicular to one of the square edges. I–V characteristics were measured at 4.2 K and in Figure 6.6 I show the dependence of I_c on the applied field, H.

Each device has an aluminum layer about 200 Å thick, and both have AlO_x layers grown *in situ* via co-deposition. The devices shown are both 30×30 μm^2. The field-dependence of I_c takes the familiar Fraunhofer form predicted by Josephson [64]. Gurvitch *et al.* observed a similar field-dependence for Nb/Al-oxide-Al/Nb junctions 20 μm in size [5]. The periodicity in the field, ΔH, can be related to the flux quantum, $\Phi_0 = hc/2e = 2.07 \times 10^{-7}$ G cm^2, through the equation:

$$\Phi_0 = \Delta H L(2\lambda + d).$$

Here, L is the width of the device edge through which the field passes, d is the barrier thickness, and 2λ is the sum of penetration depths in the bottom and top electrodes, including any finite thickness effects. Because of it's small size with respect to the penetration depths, d (~ 20 Å) can be neglected here. For $\Delta H \approx 7$ G and $L = 30$ μm, $2\lambda \approx 990$ Å. This value is comparable to that found by Maxfield *et al.* for the penetration depth in bulk niobium, $\lambda = 470$ Å [65]. However, Broom *et al.* [66] and Cucolo *et al.* [67] both report penetration depths in niobium tunnel-junctions in the range 800–1000 Å. I would also point out that I observe a larger ΔH for 30 μm junctions than Gurvitch *et al.* do for 20 μm devices [5]. For those devices they report a ΔH of about 5.5 G, which gives a value for 2λ of about 1900 Å.

The value 2λ can also be determined via measurement of resonant modes in the sub-gap tunneling structure. Because of the device geometry – two superconducting planes separated by an insulating layer – tunnel-junctions can behave like open-ended resonators. Nonlinear interactions between the resonant modes of the cavity and the ac Josephson effect can give rise to a dc current through the junction. This interaction is enhanced by spatial modulation of the Josephson current through the application of an external magnetic field. These modes appear at finite bias, in the sub-gap region of the I–V curve, with zero differential resistance. In Figure 6.7 I

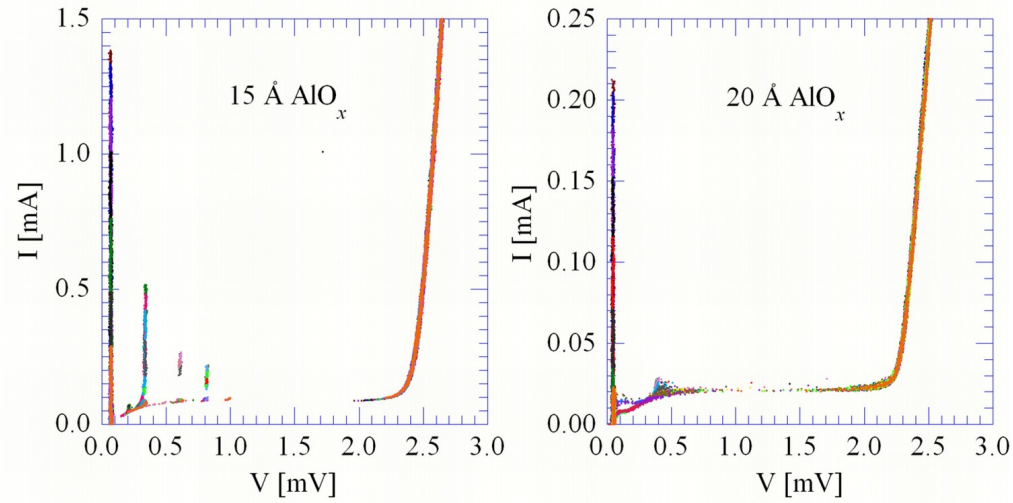

Figure 6.7: Fiske modes for applied fields up to 16 G. Devices shown here are the same as those shown in Figure 6.6.

show I–V characteristics demonstrating these modes for applied fields ranging from 0–16 G. These modes were first observed by Fiske and Coon in Sn/Sn and Sn/Pb tunnel-junctions[68, 69], and are thus commonly referred to as Fiske modes. The theory of these steps was first described by Eck *et al.* [70] and Kulik [71].

The devices shown in Figure 6.7 are the same as those shown in Figure 6.6 – one has 15 Å co-deposited AlO_x and the other 20 Å. What's immediately clear from the I–V plots is the effect that junction transparency has on the amplitude of the Fiske modes. For the thicker-barrier device only the 1st-order Fiske mode is visible, and just barely so. On the other hand, the 15 Å device shows Fiske modes out to 3rd-order. Also evident in Figure 6.7 is the decreasing amplitude near the half-gap voltage and a decreasing spacing between modes. Both of these features can be attributed to high-frequency effects [69].

The voltages, V_n, at which Fiske modes occur are related to the quantity 2λ. Electromagnetic waves have a phase velocity, v_{ph}, between the superconducting electrodes of

$$v_{ph} = c\sqrt{\frac{d}{\varepsilon_r(2\lambda + d)}},$$

where ε_r is the dielectric constant of the insulating layer. The wavelength of a standing wave is simply $2L/n$, and the frequency, f, corresponds to a Josephson frequency,

$$f = \frac{2eV_n}{h}.$$

The characteristic voltages, V_n, of the Fiske resonances can then be expressed as

$$V_n = \frac{nhv_{ph}}{4eL} = \frac{nhc}{4eL}\sqrt{\frac{d}{\varepsilon_r(2\lambda + d)}}.$$

For the 15 Å device, the 1st- and 2nd-order Fiske steps occur at multiples of 0.27 mV. This voltage step agrees quite well with what Gijsbertson *et al.* [72] and Sugiyama *et al.* [73] report for similar-sized Nb/AlO_x/Nb junctions. $V_1 = 0.27$ mV gives a Josephson frequency of 130 GHz and a phase velocity, $v_{ph} = 0.026c$. Letting $L = 30$ μm, $d = 15$ Å, and $\varepsilon_r \approx 10$, the resulting value for 2λ is approximately 2200 Å. While this is roughly twice as large as the 2λ value found from the Fraunhofer pattern, it does agree well with what's been reported in the literature [66, 67, 5]. I suspect that this discrepancy is likely due to field screening from the semi-infinite base electrode due to the Meissner effect. A lower applied field would correspond to a larger value for 2λ as derived from the critical-current field dependence.

The amplitudes of the Fiske modes are also predicted to be field dependent, as shown by Kulik [71]. The field dependence is described by the function $F_n^2(H/\Delta H)$, where again ΔH is the field periodicity of the Fraunhofer pattern, and the function $F_n(x)$ is given by

$$F_n(x) = \frac{2}{\pi}\frac{x}{|x^2 - (n/2)^2|} \times \begin{cases} |\cos(\pi x)| & n = 1, 3, 5, \ldots \\ |\sin(\pi x)| & n = 2, 4, 6, \ldots \end{cases}$$

The function $F_n^2(x)$ gives the maximum intensity for the first three Fiske modes at

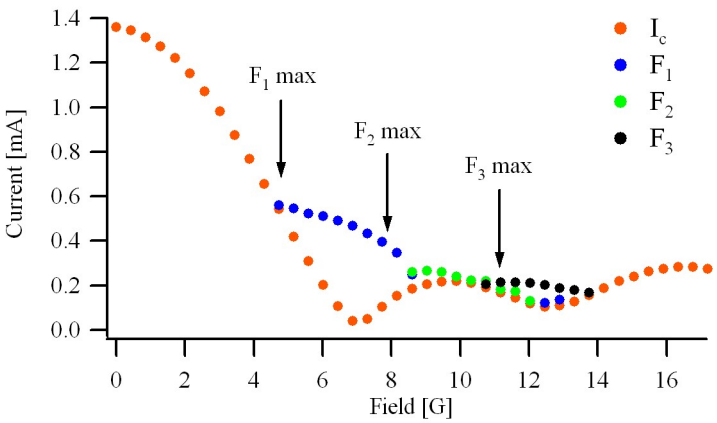

Figure 6.8: I_c versus applied field, as well as the amplitudes of the first three Fiske modes, F_n, as a function of H for the 3. The theoretical maxima of the Fiske modes are indicated by the arrows, and found to agree quite well with the data.

0.68, 1.13, and 1.59 times ΔH, respectively. In Figure 6.8 I show the amplitudes of the Fiske resonances, along with I_c. The positions of the Fiske-mode maxima agree quite well with my data. Gijsbertson *et al.* [72] also found good agreement between the amplitudes of observed Fiske resonances and the theory of Kulik [71]. They were able to isolate individual modes and fit several oscillations to the functions F_n.

Not only do I find good agreement with theory in regards to the field dependence of the Fiske modes, but also in the voltage dependence of the sub-gap current. Because measurements are made at a finite temperature ($T = 4.2$ K) there exist thermally excited quasi-particles in both superconducting electrodes. At voltages smaller than the energy gap sum, $\Delta_1 + \Delta_2$, these thermal excitations will give rise to a finite current across the junction. While in general terms this current can only be found by integrating over the densities of states on either side of the junction, for the special case where $\Delta_1 = \Delta_2 = \Delta$ and $k_B T \ll \Delta$, the sub-gap current, I_{sg}, can be well approximated by [74]:

$$I_{sg} = \frac{2G_n}{e} e^{-\Delta/k_B T}(eV + \Delta)\sqrt{\frac{2\Delta}{eV + 2\Delta}} \sinh\left(\frac{eV}{2k_B T}\right) K_0\left(\frac{eV}{2k_B T}\right) \qquad (6.1)$$

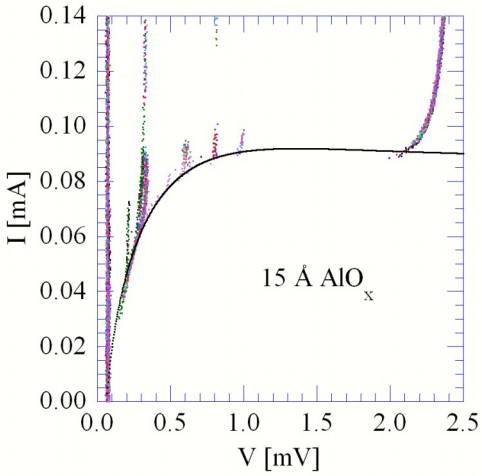

Figure 6.9: Sub-gap current for a 30 × 30 μm^2 junction with 15 Å of co-deposited AlO_x. The black curve is a fit to Eqn. 6.1, with fitting parameters described in the text.

where G_n is the normal-state conductance and K_0 is the zeroth-order modified Bessel function. For the device with 15 Å of co-deposited AlO_x I show the fit to Equation 6.1 in Figure 6.9. With G_n fixed to its measured value of 1.3 S, I found $\Delta = 1.2$ eV, which corresponds well with the steep current increase at about 2.4 eV. The agreement with theory is quite remarkable considering that the condition, $\Delta_1 = \Delta_2$, is surely not satisfied due to the 200 Å of Al metal on one side of the junction. It also suggests that the measured characteristics of my devices is limited by temperature and not by materials.

6.3 Summary

I have grown epitaxial Nb/Al bi-layers on A-plane sapphire substrates. Al (111) was found to grow in the Nishiyama-Wassermann orientation on the Nb (110) surface, in accordance with previous findings. Both RHEED and AFM indicated an initial island-growth mode that persisted until enough aluminum was deposited to completely wet the niobium surface. XRD measurements confirmed the single-crystal

nature of the bi-layers, and also revealed the orientational relationship and Al twinning.

For the first time, epitaxial Nb/Al bi-layers grown by MBE were employed in the fabrication of Josephson tunnel-junctions. Aluminum oxide tunnel-barriers were formed in a variety of ways on Al films that ranged in thickness from 200–470 Å. I-V characteristics showed a dependence on both the Al thickness and the method of oxide formation. Applied magnetic fields were shown to have the expected effect on I_c and Fiske modes were observed. Even though there was some disagreement in the measured penetration depth, the Fiske resonances exhibited maxima in the same locations predicted by theory. Finally, I found that the sub-gap current in my devices agrees well with theory, suggesting that the measured device characteristics are limited by the presence of thermally excited quasi-particles and not by materials. The device results have added significance because of the fabrication technique – epitaxial bi-layers and multi-layers allow for tunneling and proximity effect experiments to be carried out in the clean limit.

Chapter 7

Directions for Future Research

I see a number of potential directions for future research involving epitaxial aluminum oxide, both in materials research and in device fabrication. I also think the device results from oxidized epitaxial aluminum layers suggest some promising new experiments. Some ideas are presented here.

First, there has been a lot of work done concerning the accommodation of misfit in hetero-epitaxial thin films and multi-layers. The vast majority of experimental studies have been done with semiconductors though – strain and plastic deformation are of great concern to anyone making electronic devices – with none performed on epitaxial oxide films on refractory metals. Because we are trying to make both structurally and electrically perfect tri-layers, misfit strain and the possible generation of dislocations is important to understand. The new high-resolution TEM in the CMM may be a great tool for observing dislocations in thin Al_2O_3 films and developing that understanding.

Second, we can take some cues from the work of Oh *et al.* Using aluminum metal as the counter-electrode may eliminate the degradation of the oxide barrier. It may also be sufficient to coat the oxide with only 50 Å or so of aluminum to protect the barrier, and then deposit more niobium. In the end though it may be that the oxide, with its misfit-induced strain, is still electrically "leaky". Deposition of the barrier at room temperature followed by crystallization at higher temperatures might result in an unstrained layer, with any misfit dislocations confined to the interface with the base niobium. The most straightforward way to eliminate dislocations though is to

simply eliminate the misfit altogether by choosing compatible materials. Alumina growth on Nb (111) nearly accomplishes this – the misfit there is a uniform 2%.

Third, a more extensive study of epitaxial aluminum metal layers in tunnel-junctions might be interesting. Examination of device characteristics as a function of aluminum thickness could give insight into proximity effects in the clean limit. Changes in the growth parameters may also allow for the deposition of thinner continuous aluminum films. It would also be worthwhile to explore higher applied fields, and vary the oxidation levels to produce barriers of different transparencies. Devices with more transparent barriers could also be expected to show stronger Fiske resonances as well. A related experiment might involve replacing the first 100 Å or so of epitaxial aluminum with a isomorphic material such as gold or nickel.

Finally, all of these experiments – both those reported on and those proposed – could be repeated using chromium instead of aluminum. The primary interest there, of course, is in the antiferromagnetic properties of chromium and its oxide, Cr_2O_3 (chromia), and their interaction with superconducting niobium. Chromia takes the same corundum structure as alumina, and its hetero-epitaxy would provide a complementary data set with which to compare and contrast. Unlike alumina though, chromia is a semiconductor, but could still serve as a barrier for tunneling experiments. And because chromium metal grows epitaxially on niobium, thin metallic layers could be deposited and then oxidized, just as with aluminum. Chromium metal itself could be used in a superconductor–normal metal–superconductor (SNS) junction. Then different orientations of the chromium layer could be grown by choosing the appropriate substrate, and the orientation of the spin-density wave and its effects on tunneling could be studied.

References

[1] M. A. Nielson and I. L. Chuang. *Quantum Computation and Quantum Information.* Cambridge University Press, Cambridge (2000).

[2] D. J. van Harlingen, T. L. Robertson, B. L. T. Plourde, P. A. Reichardt, T. A. Crane, and J. Clarke. *Decoherence in Josephson-Junction Qubits Due to Critical-Current Fluctuations.* Phys. Rev. B **70**, 064517 (2004).

[3] I. Martin, L. Bulaevskii, and A. Shnirman. *Tunneling Spectroscopy of Two-Level Systems Inside a Josephson Junction.* Phys. Rev. Lett. **95**, 127002 (2005).

[4] J. M. Martinis, K. B. Cooper, R. McDermott, M. Steffen, M. Ansmann, K. D. Osborn, K. Cicak, S. Oh, D. P. Pappas, R. Simmonds, and C. C. Yu. *Decoherence in Josephson Qubits from Dielectric Loss.* Phys. Rev. Lett. **95**, 210503 (2005).

[5] M. Gurvitch, M. A. Washington, and H. A. Huggins. *High Quality Refractory Josephson Tunnel Junctions Utilizing Thin Aluminum Layers.* Appl. Phys. Lett. **42**, 472 (1983).

[6] S. M. Durbin, J. E. Cunningham, and C. P. Flynn. *Growth of Single-Crystal Metal Superlattices in Chosen Orientations.* J. Phys. F: Met. Phys. **12**, L75 (1982).

[7] P. M. Reimer, H. Zabel, C. P. Flynn, and J. A. Dura. *Structural Characterization of Nb on Sapphire as a Buffer Layer for MBE Growth.* J. Cryst. Growth **127**, 643 (1993).

[8] C. Dietrich, B. Koslowski, and P. Ziemann. *Ultrathin Epitaxial Al_2O_3 Films Grown on Nb(110)/Sapphire(0001) Investigated by Tunneling Spectroscopy and Microscopy.* J. Appl. Phys. **97**, 083515 (2005).

[9] P. B. Welander and J. N. Eckstein. *Strained Single-Crystal Al_2O_3 Grown Layer by Layer on Nb (110) Thin Films.* Appl. Phys. Lett. **51**, 1010 (1929).

[10] P. J. Chen and D. W. Goodman. *Epitaxial Growth of Ultrathin Al_2O_3 Films on Ta(110).* Surf. Sci. Lett. **312**, L767 (1994).

[11] M.-C. Wu and D. W. Goodman. *Particulate Cu on Ordered Al_2O_3: Reactions with Nitric Oxide and Carbon Monoxide.* J. Phys. Chem. **98**, 9874 (1994).

[12] J. Günster, M. Brause, T. Mayer, A. Hitzke, and V. Kempter. *Growth of Ultrathin Alumina Films on W(110).* Nuc. Instr. and Meth. in Phys. Res. B **100**, 411 (1995).

[13] S. Oh, K. Cicak, J. S. Kline, M. A. Sillanpää, K. D. Osborn, J. D. Whittaker, R. W. Simmonds, and D. P. Pappas. *Elimination of Two Level Fluctuators in Superconducting Quantum Bits by an Epitaxial Tunnel Barrier.* Phys. Rev. B **74**, 100502 (2006).

[14] G. V. Samsonov. *The Oxide Handbook.* IFI/Plenum Data, New York (1982).

[15] S. Oh, D. A. Hite, K. Cicak, K. D. Osborn, R. W. Simmonds, R. McDermott, K. B. Cooper, M. Steffen, J. M. Martinis, and D. P. Pappas. *Epitaxial Growth of Rhenium with Sputtering.* Thin Solid Films **389**, 496 (2006).

[16] L. Pauling. *The Crystal Structures of Hematite and Corundum.* J. Am. Chem. Soc. **47**, 781 (1925).

[17] M. L. Kronberg. *Plastic Deformation of Single Crystals of Sapphire: Basal Slip and Twinning.* Acta Metal. **5**, 507 (1957).

[18] R. E. Newnham and Y. M. de Haan. *Refinement of the α Al_2O_3, Ti_2O_3, V_2O_3 and Cr_2O_3 Structures.* Z. Krist. **117**, 235 (1962).

[19] W. E. Lee and K. P. D. Lagerlof. *Structural and Electron Diffraction Data for Sapphire (α-Al_2O_3).* J. Elec. Micros. Tech. **2**, 247 (1985).

[20] Y. V. Shvyd'ko, M. Lucht, E. Gerdau, M. Lerche, E. E. Alp, W. Sturhahn, J. Sutter, and T. S. Toellner. *Measuring Wavelengths and Lattice Constants with the Mössbauer Wavelength Standard.* J. Synchrotron Rad. **9**, 17 (2002).

[21] I. Levin and D. Brandon. *Metastable Alumina Polymorphs: Crystal Structures and Transition Sequences.* J. Am. Ceram. Soc. **81**, 1995 (1998).

[22] O. Hellwig, K. Theis-Bröhl, G. Wilhelmi, H. Zabel, and A. Stierle. *Temperature and Thickness Dependent Epitaxial Relationship of Pd (111) on Cr (110).* Thin Solid Films **318**, 201 (1998).

[23] G. Wassermann. Arch. Eisenhüttenwesen **126**, 647 (1933).

[24] Z. Nishiyama. Sci. Rep. Tohoku Univ. **23**, 638 (1934).

[25] G. Kurdjumov and G. Sachs. *On the Mechanism of Steel Hardening.* Z. Phys. **64**, 325 (1930).

[26] L. A. Bruce and H. Jaeger. *Geometric Factors in f.c.c. and b.c.c. Metal-on-Metal Epitaxy III. The Alignments of (111) f.c.c.-(110) b.c.c. Epitaxed Metal Pairs.* Phil. Mag. A **38**, 223 (1978).

[27] R. Ramirez, A. Rahman, and I. K. Schuller. *Epitaxy and Superlattice Growth.* Phys. Rev. B **30**, 6208 (1984).

[28] E. Bauer and J. H. van der Merwe. *Structure and Growth of Crystalline Superlattices: From Monolayer to Superlattice.* Phys. Rev. B **33**, 3657 (1986).

[29] Y. Gotoh and H. Fukuda. *Interfacial Energy of the bcc (110)/fcc (111) Interface and Energy Dependence on its Size.* Surf. Sci. **223**, 315 (1989).

[30] D. W. Goodman. *Chemical and Spectroscopic Studies of Metal Oxide Surfaces.* J. Vac. Sci. Technol. A **14**, 1526 (1996).

[31] C. Dietrich, H.-G. Boyen, and B. Koslowski. *Characterization of Ultrathin Insulating Al_2O_3 Films Grown on Nb(110)/Sapphire(0001) by Tunneling Spectroscopy and Microscopy.* J. Appl. Phys. **94**, 1478 (2003).

[32] Y. S. Dedkov and M. Fonin. *Preparation of the Subnanometer Thick Epitaxial Al_2O_3 (0001) Layers on Fe (110) for Magnetic Tunnel Junctions.* Appl. Surf. Sci **253**, 3860 (2007).

[33] A. I. Braginski, J. Talvacchio, M. A. Janocko, and J. R. Gavaler. *Crystalline Oxide Tunnel Barriers Formed by Thermal Oxidation of Aluminum Overlayers on Superconductor Surfaces.* J. Appl. Phys. **60**, 2058 (1986).

[34] E. C. G. Kirk, M. G. Blamire, R. E. Somekh, and J. E. Evetts. *The Influence of Al Morphology on Quality in Nb/Al/AlO_x/Al/Nb Epitaxial Base Layer Junctions.* IEEE Trans. Appl. Supercond. **3**, 2178 (1993).

[35] S. Oh, K. Cicak, R. McDermott, K. B. Cooper, K. D. Osborn, R. W. Simmonds, M. Steffen, J. M. Martinis, and D. P. Pappas. *Low-Leakage Superconducting Tunnel Junctions with a Single-Crystal Al_2O_3 Barrier.* Supercond. Sci. Technol. **18**, 1396 (2005).

[36] A. R. Wildes, J. Mayer, and K. Theis-Bröhl. *The Growth and Structure of Epitaxial Niobium on Sapphire.* Thin Solid Films **401**, 7 (2001).

[37] I. K. Schuller. *New Class of Layered Materials.* Phys. Rev. Lett. **44**, 1597 (1980).

[38] S. M. Durbin, J. E. Cunningham, M. E. Mochel, and C. P. Flynn. *Nb-Ta Metal Superlattices.* J. Phys. F: Met. Phys. **11**, L223 (1981).

[39] J. H. Claassen, S. A. Wolf, S. B. Qadri, and L. D. Jones. *Epitaxial Growth of Niobium Thin Films.* J. Cryst. Growth **81**, 557 (1987).

[40] J. Mayer, C. P. Flynn, and M. Rühle. *High-Resolution Electron Microscopy Studies of Nb/Al_2O_3 Interfaces.* Ultramicroscopy **33**, 51 (1990).

[41] G. Gutekunst, J. Mayer, and M. Rühle. *Atomic Structure of Epitaxial Nb-Al_2O_3 Interfaces I. Coherent Regions.* Phil. Mag. A **75**, 1329 (1997).

[42] T. Wagner. *High Temperature Epitaxial Growth and Structure of Nb Films on $\alpha Al_2O_3(0001)$.* J. Mater. Res. **13**, 693 (1998).

[43] T. Wagner, M. Lorenz, and M. Rühle. *Thermal Stability of Nb Thin Films on Sapphire.* J. Mater. Res. **11**, 1255 (1996).

[44] C. Sürgers and H. v. Löhneysen. *Effect of Oxygen Segregation on the Surface Structure of Single-Crystalline Niobium Films on Sapphire.* Appl. Phys. A **54**, 350 (1992).

[45] T. W. Haas, A. G. Jackson, and M. P. Hooker. *Adsorption on Niobium (110), Tantalum (110), and Vanadium (110) Surfaces.* J. Chem. Phys. **46**, 3025 (1967).

[46] M. Ondrejcek, R. S. Appleton, W. Swięch, V. L. Petrova, and C. P. Flynn. *Thermally Activated Stripe Reconstruction Induced by O on Nb(011).* Phys. Rev. Lett. **87**, 116102 (2001).

[47] K. Pantel, M. Bujor, and J. Bardolle. *Continuous Measurement of Surface Potential Variations During Oxygen Adsorption on the (100), (110) and (111) Faces of Niobium Using Mirror Electron Microscope.* Surf. Sci. **62**, 589 (1977).

[48] I. Arfaoui, J. Cousty, and H. Safa. *Tiling of a Nb (110) Surface With NbO Crystals Nanosized by the NbO/Nb Misfit.* Phys. Rev. B **65**, 115413 (2002).

[49] I. Arfaoui, J. Cousty, and C. Guillot. *A Model of the $NbO_{x\approx 1}$ Nanocrystals Tiling a Nb (110) Surface Annealed in UHV.* Surf. Sci. **557**, 119 (2004).

[50] C. P. Flynn. *Constraints on the Growth of Metallic Superlattices.* J. Phys. F: Met. Phys. **18**, L195 (1988).

[51] C. P. Flynn and W. Swięch. *Periodic States in the Constrained Equilibrium of Vicinal Nb (011) Miscut along [100].* Phys. Rev. Lett. **83**, 3482 (1999).

[52] C. P. Flynn, W. Swięch, R. S. Appleton, and M. Ondrejcek. *Nanofaceting of Vicinal Nb (011).* Phys. Rev. B **62**, 2096 (2000).

[53] S. A. Wolf, S. B. Qadri, J. H. Claassen, T. L. Francavilla, and B. J. Dalrymple. *Epitaxial Growth of Superconducting Niobium Thin Films by Ultrahigh Vacuum Evaporation.* J. Vac. Sci. Technol. A **4**, 524 (1986).

[54] G. Oya, M. Koishi, and Y. Sawada. *High-Quality Single-Crystal Nb Films and Influences of Substrates on the Epitaxial Growth.* J. Appl. Phys. **60**, 1440 (1986).

[55] W. DeSorbo. *Effect of Dissolved Gases on Some Superconducting Properties of Niobium.* Phys. Rev. **132**, 107 (1963).

[56] G. W. Webb. *Low-Temperature Electrical Resistivity of Pure Niobium.* Phys. Rev. **181**, 1127 (1969).

[57] K. G. Tscherich and V. von Bonin. *Formation of an Atomic Hydrogen Beam by a Hot Capillary.* J. Appl. Phys. **84**, 4065 (1998).

[58] W. M. Mullins and B. L. Averbach. *Bias-Reference X-ray Photoelectron Spectroscopy of Sapphire and Yttrium Aluminum Garnet Crystals.* Surf. Sci. **206**, 29 (1988).

[59] W. M. Yim and R. J. Paff. *Thermal Expansion of AlN, Sapphire and Silicon.* J. Appl. Phys. **45**, 1456 (1974).

[60] P. Aldebert and J.-P. Traverse. *α-Al_2O_3: A High-Temperature Thermal Expansion Standard.* High Temps. High Pressures **16**, 127 (1984).

[61] Y. S. Touloukian, R. K. Kirby, R. E. Taylor, and P. D. Desal. *Thermophysical Properties of Matter, Vol. 12.* IFI/Plenum Data, New York (1975).

[62] H. J. Tao, E. D. Gibson, J. D. Verhoeven, and E. L. Wolf. *Combined Tunnelling and SEM Channelling Analysis of Metallic Bilayers Al (111) Epitaxed on Nb (110).* Phil. Mag. B **50**, L55 (1984).

[63] S. Yamamoto and H. Naramoto. *RBS/Channeling Analysis of Epitaxial Films With Nb Buffer Layer on Sapphire Substrate.* Nucl. Instr. and Meth. B **190**, 657 (2002).

[64] B. D. Josephson. *Possible New Effects in Superconductive Tunnelling.* Phys. Lett. **1**, 251 (1962).

[65] B. W. Maxfield and W. L. McLean. *Superconducting Penetration Depth of Niobium.* Phys. Rev. **139**, A1515 (1965).

[66] R. F. Broom. *Some Temperature-Dependent Properties of Niobium Tunnel Junctions.* J. Appl. Phys. **47**, 5432 (1976).

[67] A. M. Cucolo, S. Pace, R. Vaglio, A. D. Chiara, G. Peluso, and M. Russo. *Magnetic Field Penetration in Niobium- and Vanadium-Based Josephson Junctions.* J. Low Temp. Phys. **50**, 301 (1983).

[68] M. D. Fiske. *Temperature and Magnetic Field Dependences of the Josephson Tunneling Current.* Rev. Mod. Phys. **36**, 221 (1964).

[69] D. D. Coon and M. D. Fiske. *Josephson ac and Step Structure in the Supercurrent Tunneling Characteristic.* Phys. Rev. **138**, A744 (1965).

[70] R. E. Eck, D. J. Scalapino, and B. N. Taylor. *Self-Detection of the ac Josephson Current*. Phys. Rev. Lett. **13**, 15 (1964).

[71] I. O. Kulik. *Theory of "Steps" of Voltage-Current Characteristic of the Josephson Tunnel Current*. JETP Lett. **2**, 84 (1965).

[72] J. G. Gijsbertsen, E. P. Houwnian, J. Flokstra, H. Rogalla, J. B. le Grand, and P. A. J. de Korte. *Field Dependence of Fiske Resonances in Nb-AlO_x Based Josephson Junctions*. IEEE Trans. Appl. Supercond. **3**, 2100 (1993).

[73] H. Sugiyama, A. Fujimaki, and H. Hayakawa. *Characteristics of High Critical Current Density Josephson Junctions with Nb/AlO_x/Nb Trilayers*. IEEE Trans. Appl. Supercond. **5**, 2739 (1995).

[74] T. V. Duzer and C. W. Turner. *Principles of Superconductive Devices and Circuits*. Elsevier, New York (1981).

Author's Biography

Paul Brent Welander was born in Portland, Oregon, on August 12, 1976, to parents Gary and Barbara Welander. He has three younger brothers: Benjamin, Adam and Matthew. On July 24, 1999, Paul married Paula Veronica Aguirre in Los Angeles, Calfornia. Together, Paul and Paula have two children, both born in Urbana, Illinois: a daughter, Katherine Elena, born April 19, 2004, and a son, Daniel Brent, born June 26, 2006.

Paul received his diploma from Central High School in Independence, Oregon, in June 1994. That same fall, he began his baccalaureate studies at Occidental College in Los Angeles, California, taking up Physics as his major. As part of a 3/2 program, he transferred to the California Institute of Technology in Pasadena, California, in the fall of 1997. There, Paul studied Engineering and Applied Sciences, and in June 1999 he received both a B.A. from Occidental College and a B.S. from the California Institute of Technology.

During the period from January 1997 to July 2001, Paul worked as a Research Assistant with the Low Temperature Science and Engineering Group at the Jet Propulsion Laboratory in Pasadena, California. His research included the development of a new miniature high-resolution thermometer for low-temperature applications. Paul also worked for a brief time on an experiment designed to observe Josephson effects in superfluid helium-4. Concurrent with his research at the Jet Propulsion Laboratory, Paul worked part-time at his alma mater, Occidental College, as an Adjunct Instructor of Physics from August 1999 to May 2001. He taught

laboratory courses in Introductory Mechanics and Electromagnetics.

In August, 2001, Paul began his doctoral studies in Physics at the University of Illinois at Urbana-Champaign. He worked with the research group of Ali Yazdani for one semester before joining the Eckstein group in the summer of 2002. In addition to the research described in this thesis, Paul also briefly studied the epitaxy of dilute ferromagnets on niobium, as well as superconducting proximity effects at epitaxial niobium-chromium interfaces.

Upon graduation, Paul will join the technical staff of the Analog Device Technology group at MIT Lincoln Laboratories in Lexington, Massachusetts.